

High efficiency Josephson Ratchet Based on YBCO Josephson Junction Fabricated with a Focused He-Ion Beam

EBERHARD KARLS
UNIVERSITÄT
TÜBINGEN



Physikalisches Institut

by

Alireza Jozani

Supervised by Prof. Dr. **Edward Goldobin**

Jun, 2023



To my beloved parents

Contents

Introduction	1
1 Josephson effect	3
1.1 Josephson Junction	3
1.2 Current Voltage Characteristic (IVC)	7
1.3 Josephson Junction in a Magnetic Field	9
2 Theory of Ratchet	12
2.1 An Overview of Josephson Ratchet	12
2.1.1 Josephson Ratchet Operation	14
2.1.2 Efficiency	17
2.1.3 Junctions of In-line Geometry	19
3 Fabrication and Implementation	23
3.1 Sample Information	23
3.2 Sample Layout	23
3.3 Sample Fabrication	24
3.4 He-FIB	26
3.5 Characterization	27
3.6 Implementation of an In-line Geometry Josephson Ratchet	30
4 Experimental Results	33
4.1 An Overview	33
4.2 Josephson Ratchet A22	33
4.2.1 Experimental Simulation of A22	41
4.3 Josephson Ratchet A15	44
4.4 Driving the Ratchet with a Stochastic Signal	49
4.4.1 External noise	50
4.4.2 Internal noise	52
4.5 Conclusion and Outlook	55

List of Tables

3.1	The maximum I_c is determined by measuring $I_c(H)$ and selecting the highest value, which may be reduced when $I_{\text{coil}} \neq 0$.	28
3.2	Comparison table of target parameters between ratchet A15 and A22.	32
4.1	Comparison table of target and actual parameters of ratchet A22. Notice that we chose $\lambda = 250 \text{ nm}$ and subsequently $\lambda_{\text{eff}} = 2 \mu\text{m}$.	33
4.2	Comparison table of target and actual parameters of ratchet A15.	44
4.3	Comparison table of important parameters for a system with a periodic asymmetric potential. ALJJ is the abbreviation of annular long JJ, and SQUID is the abbreviation of superconducting quantum interference device. Note that in the ref Knufinke et al [1]., they just obtained \bar{V}_{dc} experimentally, while simulating all the other parameters using a custom-made asymmetric IVC.	55

List of Figures

1	(a) An example of a particle trapped in a schematic asymmetric potential (b) Schematically indicates the meaning of asymmetric.	1
2	The in-line geometry of a (JJ) consists of superconducting where the dashed line represents the barrier JJ surrounded by superconductors. The arrows indicate the current I flowing through the superconductors.	2
1.1	A JJ made by the barrier potential insulator, which is formed by two closely spaced superconductors on the left and right.	3
1.2	Schematic electronic equivalent circuit of JJ and a RCSJ.	5
1.3	Plots of the tilted washboard potential $U(\varphi)$ are shown for several values of the tilt (bias current) γ . When $\gamma < 1$, the phase particle is trapped in the minimum of the potential. However, when $\gamma \geq 1$, the particle escapes from the minimum and slides down the potential.	7
1.4	Current-Voltage Characteristic (IVC) of a symmetric potential.	8
1.5	Negative and positive $I_c(\Phi_J)$ are symmetric for a fixed Φ_J . For example, when the value of Φ_J/Φ_0 is fixed at 44.5, we observe, $ I_{c+}/I_0 = I_{c-}/I_0 = 0.75$.	11
2.1	(a) An example of a particle trapped in a schematic asymmetric potential (b) Schematically indicates the meaning of asymmetric.	12
2.2	The schematic example shows an asymmetric non-hysteretic IVC for an asymmetric Josephson potential. I_{c+} represents the positive critical current, and I_{c-} represents the negative critical current.	13
2.3	A rectification curve represents the average velocity of a particle ($\langle \dot{\varphi} \rangle \propto V$) as a function of the applied ac-drive amplitude I_{ac} . The interval between I_{c+} and I_{c-} is called operation interval or the rectification window, which can be defined as $\Delta \equiv I_{c-} - I_{c+}$.	14
2.4	A ratchet potential for $I_{dc} = 0, I_{c-}, I_{c+}$.	15
2.5	The schematic loaded ratchet up to countercurrent $ I_{dc} = 0.2 \mu\text{A}$.	16
2.6	(a) A custom-made asymmetric IVC with $\mathcal{A} = 4$. (b) The rectification curves for several values of I_{dc} based on the asymmetric IVC, borrowed from [1].	16
2.7	(c) Average input ac power \bar{P}_{in} , (d) average output dc power \bar{P}_{out} , (e) efficiency η , fig(4) of [1].	18

2.8	(a) The in-line geometry of a (JJ) consists of superconducting where the dashed line represents the barrier JJ surrounded by superconductors. The arrows indicate the current I flowing through the superconductors. (b) The current density j_L as a function of distance x .	19
2.9	A family of asymmetric $I_c(f)$ for different f^M obtained by solving the eq. (2.4) numerically.	21
2.10	(a) Asymmetry parameter \mathcal{A} vs. magnetic flux f for different values of f^M (b) Asymmetry parameter \mathcal{A} vs. strength of in-line geometry f^M .	22
3.1	YBCO film on 2 inch LSAT substrate. (a) The scanning electron microscope picture of the sample surface. The critical temperature T_c and the value of the current density j_c are provided by Ceraco. (b) A schematic picture of the chip showing the deposition of its different layers.	23
3.2	the layout of the small chip. The hatched light green areas correspond to the Au covered pads, while the blue areas represent the LSAT substrate. The guide lines are also covered by Au, and the Au layer is removed down to YBCO on the bridges.	24
3.3	Masks used during the patterned process: (a) Mask used during step (i) for the etching of gold. The blue zone indicates where the gold has been removed, leaving only YBCO. The yellow zones indicate where the gold still remains. (b) The mask used during step (ii) for the etching of YBCO. The areas in blue represent the regions where the YBCO still remains. The black area represents LSAT (substrate). Note that in the regions where the gold remains from the first step (e.g., over the pads), it has not been removed during the second step.	25
3.4	The microscope pictures of the sample after each step of the lithography process: (a) Picture of the pads after the step (i). The dark areas represent YBCO, and the yellow areas represent gold. (b) The picture of the bridges after the step (ii). The yellow area represents gold, the dark area represents LSAT, the blue area represents YBCO where the junction will be finally irradiated, and the purple lines are guide lines for our next step using He-FIB.	25
3.5	The poster of He-FIB.	26
3.6	(a) The red line indicates focused He ion beam on the atomic level with a width of the order of a few nm. (b) Schematic sketch of the BJJ produced by He-FIB, where the red line indicates the barrier JJ.	27
3.7	BJJs characterization of $j_c(D)$ experimental data and fit. 11 BJJ's with the dose $D \approx 450\ldots700$ ionS/nm. The width of the BJJ's is $W = 2.8\text{ }\mu\text{m}$ and the film thickness $d = 30\text{ nm}$.	28
3.8	IVC and $I_c(H)$ of junction B28 with $D = 350$ ionS/nm.	29
3.9	IVC and $I_c(H)$ of junction D19 with dose $D = 450$ ionS/nm.	29
3.10	IVC and $I_c(H)$ of junction D22 with dose $D = 505$ ionS/nm.	29
3.11	IVC and $I_c(H)$ of junction B33 with dose $D = 600$ ionS/nm.	30

3.12 Sketch of the Josephson ratchet. The blue zone is YBCO, the red solid lines are the resistive walls, dash red line is the BJJ, and arrows indicate the flow of the supercurrent through the Josephson ratchet. w is the distance between two resistive walls and L is the length of BJJ.	30
4.1 IVC of the ratchet A22 at $I_{\text{coil}} = 0$ where $ I_{c+} \approx I_{c-} \approx 8.43 \mu\text{A}$.	34
4.2 Critical current versus magnetic coil current of the Josephson ratchet A22. We used a voltage criterion equal to $1 \mu\text{V}$ for this measurement.	35
4.3 Value of asymmetry parameter dependence of I_{coil} , which shows the maximum asymmetry, is $\mathcal{A} \approx 7$ at the value of $I_{\text{coil}} \approx -69 \text{ mA}$.	36
4.4 asymmetric IVC of the ratchet A22 at the optimum magnetic field (coil current) $I_{\text{coil}} = -69 \text{ mA}$ exhibits $ I_{c+} \approx 1.53 \mu\text{A}$ and $ I_{c-} \approx -13.8 \mu\text{A}$ that makes $\mathcal{A} \approx 7$.	37
4.5 The rectification curve for the ratchet A22 at $I_{\text{coil}} = -69 \text{ mA}$ where $ I_{c-} \approx 15.2 \mu\text{A}$, $ I_{c+} \approx 2.2 \mu\text{A}$ and RW $\Delta \approx 13 \mu\text{A}$.	37
4.6 The rectification curve for the ratchet A22 at $I_{\text{coil}} = -69 \text{ mA}$ for several I_{dc} up to $ I_{\text{dc}} = 5 \mu\text{A}$.	38
4.7 (a) $\bar{P}_{\text{in}}(I)$, (b) $\bar{P}_{\text{out}}(I)$, (c) efficiency $\eta(I)$.	40
4.8 Simulations (lines) versus the experimental data (dots) of $\bar{V}_{\text{dc}}(I(t))$	42
4.9 Simulations (lines) versus the experimental data (dots) of (a) $\bar{P}_{\text{in}}(I(t))$, (b) $\bar{P}_{\text{out}}(I(t))$, and (c) $\eta(I(t))$.	43
4.10 IVC of the ratchet A15 at $I_{\text{coil}} = 0$. $ I_{c+} = I_{c-} \approx 21 \mu\text{A}$ and $R_N \approx 32 \Omega$.	45
4.11 Critical current versus magnetic coil current of the ratchet A15.	45
4.12 The value of asymmetry parameter, which shows the maximum asymmetry $\mathcal{A} \approx 7$ at optimum magnetic $I_{\text{coil}} = 75 \text{ mA}$.	46
4.13 An asymmetric IVC of the ratchet A15 at the optimum $I_{\text{coil}} = 75 \text{ mA}$ has $ I_{c-} \approx 24.5 \mu\text{A}$ and $ I_{c+} \approx 3.5 \mu\text{A}$.	46
4.14 The rectification curve for the ratchet A15 at $I_{\text{coil}} = 75 \text{ mA}$ with maximum dc average voltage $\bar{V}_{\text{dc}} \approx 225 \text{ V}$.	47
4.15 The rectification curve for the loaded ratchet A15 at $I_{\text{coil}} = 75 \text{ mA}$ for several I_{dc} up to stopping force $ I_{\text{dc}} = 8.92 \mu\text{A}$.	47
4.16 (a) \bar{P}_{in} , (b) \bar{P}_{out} , (c) efficiency η .	48
4.18 (a) The Gaussian distribution of random signal with the width σ (b) The random signal depends on time.	49
4.19 Simulation of $\bar{V}_{\text{dc}}(\sigma)$ driven with the Gaussian signal.	50
4.20 (a) $\bar{P}_{\text{in}}(\sigma)$, (b) $\bar{P}_{\text{out}}(\sigma)$, (c) and η	51
4.21 IVC of A15 at $T \approx 4.2 \text{ K}$ and 35 K at zero magnetic field $I_{\text{coil}} = 0$.	52
4.22 IVC for the ratchet A15 at around temperature 35 K for the two values of I_{coil} : zero and the optimum magnetic field. In the lower right we zoom in the origin.	53
4.23	54

Introduction

Typically, when referring to a ratchet system or equivalently Brownian motor, one can envision a system characterized by weak interaction with a surrounding large bath where symmetric nature of the potential is broken, and a periodic asymmetric potential would be immediately used to describe the ratchet system (e.g., see the schematic fig. 1). It has been demonstrated that [2], in the system where a particle is trapped in an asymmetric potential, it induces directed transport motion. This motion drives the system into a non-equilibrium state, allowing the particle to perform useful work under specific conditions. One significant effect in such a non-equilibrium state is the dominance of time-dependent perturbations, which consequently leads to a non-negligible influence of thermal noise. These effects would be captured and studied.

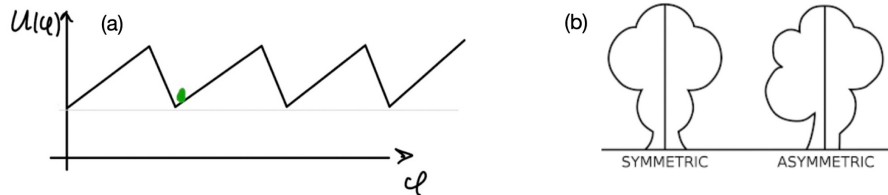


Figure 1: (a) An example of a particle trapped in a schematic asymmetric potential
(b) Schematically indicates the meaning of asymmetric.

This master's thesis focuses on the investigation of a device based on High Temperature Superconductors (HTSs), namely YBCO, where a Josephson ratchet was fabricated (designed) using a Helium focused ion Beam (He-FIB) technique. Roughly speaking, a Josephson ratchet is a device consist of an in-line geometry of a Josephson junction (e.g., see fig. 2) where a particle is trapped in an asymmetric potential.

In this thesis, the Josephson ratchet was experimentally driven in both deterministic and stochastic regimes. Subsequently, we explored the effects of external and internal noises, with a particular emphasis on the dominance of time-dependent perturbations.

As an **application**, the recent surge of interest has been focused on superconductor diodes, which serve as an equivalent realization of the Josephson ratchets. For instance, reference [3] presents a notable realization of a particle trapped within a Josephson asymmetric potential. However, in this thesis, we demonstrate that Josephson ratchets generally exhibit higher efficiency and a smaller device footprint.

The thesis is organized as follows:

In Chapter. 1, the concept of the Josephson effect with a 2π periodic gauge-invariant phase in the presence of a magnetic field is carefully examined, with a specific focus on a particle trapped in a symmetric potential.

In Chapter. 2, we will first undertake a theoretical investigation of how a particle trapped in an asymmetric Josephson potential can be operated to generate useful work with a specific level of efficiency [1] [4]. Furthermore, the dependency of critical current on the magnetic field is numerically simulated for a specific geometry (an In-line geometry of Josephson junction) to gain initial insights into the required design parameters for a Josephson ratchet.

In Chapter. 3, the focus shifts to the fabrication of the sample. The lithography process and irradiation techniques, such as He-FIB, are employed in the fabrication of the Josephson ratchet. Subsequently, we present the current density characterization of our samples.

In Chapter. 4, we present the experimental results of two Josephson ratchet devices operating in different regimes: deterministic (i.e., when the system is driven with a sinusoidal drive) and stochastic (i.e., when the Josephson ratchet is driven with a randomly varying signal, such as noise). We measure such figures of merits \bar{V}_{dc} , \bar{P}_{out} , \bar{P}_{in} , and the efficiency. Furthermore, since we operate in a quasi-static regime, we can simulate all the ratchet parameters based on the experimental current-voltage characteristics. Notably, we investigate how external noise affects the particle's dynamics in an asymmetric potential, enabling ratchet operation. Lastly, we explore the influence of internal noise, modeled as a random signal following the Gaussian distribution.

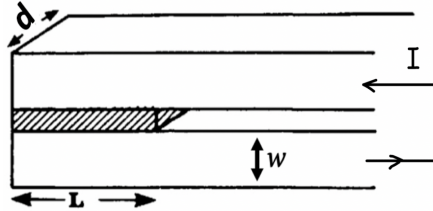


Figure 2: The in-line geometry of a (JJ) consists of superconducting where the dashed line represents the barrier JJ surrounded by superconductors. The arrows indicate the current I flowing through the superconductors.

In conclusion, we summarize our work concisely and provide an **outlook** on future research directions.

Chapter 1

Josephson effect

1.1 Josephson Junction

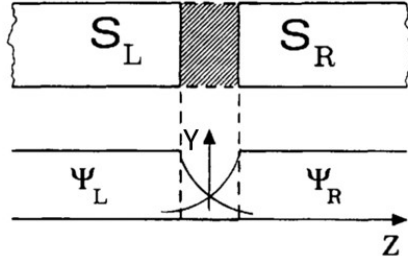


Figure 1.1: A JJ made by the barrier potential insulator, which is formed by two closely spaced superconductors on the left and right.

The Josephson effect is a phenomenon that describes the flow of supercurrent, which is a current without dissipation, between two separated superconductors. When two superconductors, denoted as S_L and S_R , are brought close together with only a small gap and a barrier separating them, a continuous supercurrent flows between them. This device is known as a Josephson junction (JJ), as shown schematically in fig. 1.1. The left superconductor has a wave function of Cooper pairs (a pair of electrons or other fermions bound together at low temperatures) $\psi_L(t, \mathbf{x}) = |\psi_0| e^{i\phi_L(t, \mathbf{x})} = \sqrt{n_{s,L}} e^{i\phi_L(t, \mathbf{x})}$.¹ Similarly, the wave function for the right superconductor, S_R , is given by $\psi_R(t, \mathbf{x}) = |\psi_0| e^{i\phi_R(t, \mathbf{x})} = \sqrt{n_{s,R}} e^{i\phi_R(t, \mathbf{x})}$. If the potential difference across the junction is V , then the potential energy difference between the two superconductors is $2eV$, since each Cooper pair has twice the charge of an electron. The Schrödinger equation for these two quantum states, ψ_L and ψ_R , is as follows

$$i\hbar \frac{\partial}{\partial t} \begin{pmatrix} \sqrt{n_{s,L}} e^{i\phi_L} \\ \sqrt{n_{s,R}} e^{i\phi_R} \end{pmatrix} = \begin{pmatrix} eV & K \\ K & -eV \end{pmatrix} \begin{pmatrix} \sqrt{n_{s,L}} e^{i\phi_L} \\ \sqrt{n_{s,R}} e^{i\phi_R} \end{pmatrix}, \quad (1.1)$$

¹Throughout this work, the bold symbol, \mathbf{x} , represents a three-dimensional vector, and ψ is a vector field which represents our wave function.

where K is an interaction coupling constant that represents the strength of the interaction coupling between the wave functions of the two superconductors, $n_{s,i}$ ($i = L$ or R) is the charge carrier density (Cooper pair density) which is proportional to the current I through the supercurrent density $\vec{j}_s = q_s \cdot n_s \cdot \vec{v}_s$, where \vec{v}_s is the velocity vector of the Cooper pairs, q_s is the Cooper charge, and S_J is the surface area of the Josephson junction, which will be precisely defined once we define the geometry of JJ later in this chapter. After taking the derivative of eq. (1.1) and splitting the real and imaginary parts, we obtain the following set of equations for ϕ_L , ϕ_R , $n_{s,L}$, and $n_{s,R}$ [5]

$$\begin{aligned}\dot{n}_{s,L} &= \frac{2K}{\hbar} \sqrt{n_{s,L} n_{s,R}} \sin(\phi_L - \phi_R), \\ \dot{n}_{s,R} &= -\frac{2K}{\hbar} \sqrt{n_{s,L} n_{s,R}} \sin(\phi_L - \phi_R),\end{aligned}\tag{1.2}$$

$$\begin{aligned}\dot{\phi}_L &= \frac{K}{\hbar} \sqrt{\frac{n_{s,L}}{n_{s,R}}} \cos(\phi_L - \phi_R) + \frac{eV}{\hbar}, \\ \dot{\phi}_R &= \frac{K}{\hbar} \sqrt{\frac{n_{s,R}}{n_{s,L}}} \cos(\phi_L - \phi_R) - \frac{eV}{\hbar}.\end{aligned}\tag{1.3}$$

The phase differences between two superconductors is defined $\varphi_0 \equiv \phi_L - \phi_R$ (without presence of a magnetic field). Thus, the differences of $\dot{\varphi}_0 \equiv \dot{\phi}_L - \dot{\phi}_R$ yields the 2nd Josephson equation as follows

$$\frac{\partial \varphi_0(t, \mathbf{x})}{\partial t} = \frac{2eV(t)}{\hbar} = \frac{2\pi V}{\Phi_0},\tag{1.4}$$

where $\Phi_0 = \frac{h}{2e} \approx 2.068 \times 10^{-15}$ Wb is magnetic flux quantum. Eq. (1.4) describes the linear evolution of phase differences across the junction for constant applied voltage. It immediately follows from eq. (1.4) that if there is no voltage across the junction i.e., $V = 0$, then φ_0 is constant. This implies constant arguments of the angular functions in eq. (1.2), and thus $\dot{n}_{s,L} = -\dot{n}_{s,R}$. Therefore, if $n_{s,L} = n_{s,R}$, then $n_{s,i} = \text{const}$, and the current should flow uniformly (in time) between the two superconductors. Otherwise, the superconductors would be charged, and the supercurrent would flow non-uniformly. Thus, the supercurrent density depends on the phase difference $j_s(\varphi_0)$, which must be gauge invariant. That is, in the presence of the magnetic field, the supercurrent density becomes as ²

$$j_s(\psi) = q_s \operatorname{Re} \left\{ \psi^* \left(\frac{\hbar}{mi} \vec{\nabla} - \frac{q_s}{m} \vec{A} \right) \psi \right\} = \frac{q_s n_s \hbar}{m_s} \vec{\nabla} \varphi,$$

where in the last equality we have inserted the definition of Cooper pair wave function and defined φ such as $\vec{\nabla} \varphi := \vec{\nabla} \varphi_0 - \frac{2\pi}{\Phi_0} \vec{A}$, which is the gauge invariant phase

²The Schrödinger equation implies the continuity equation $\left(\frac{\partial |\psi(t, \mathbf{x})|^2}{\partial t} = -\vec{\nabla} \cdot j(t, \mathbf{x}) \right)$, where the probability current density can be defined as $j_s(\psi)$. [6]

differences in the presence of magnetic field³. Now if we integrate this gauge invariant phase differences over the area of BJJ, we obtain $\varphi(t, \mathbf{x}) = \varphi_0 - \frac{2\pi}{\Phi_0} \int_L^R A_y(\mathbf{x}) dx$, where A_y is a homogeneous magnetic vector potential in the y -direction. Since φ is a gauge invariant phase, the direction of the magnetic field does not matter, but it must be perpendicular to the surface of the JJ. Additionally, we note that inside the junction, $\psi(t, \mathbf{x})$ is defined modulo 2π (i.e., $\psi(t, \mathbf{x}) = \sqrt{n_s} e^{i(\varphi(t, \mathbf{x}) + 2\pi)} = \sqrt{n_s} e^{i\varphi(t, \mathbf{x})}$), so phase changes by $2n\pi$ (n is an integer) do not change the wave function ψ . Furthermore, $j_s(\varphi)$ is time reversal invariant ($j_s(\varphi) = -j_s(-\varphi)$).

Taking all these considerations into account, we define the uniform gauge invariant supercurrent density as an odd, 2π -periodic function of the phase difference, i.e., $j_s(\varphi) = j_s(\varphi + 2n\pi)$. Thus, the first Josephson equation can be defined as follows

$$I_s := I_0 \sin [\varphi(t)]. \quad (1.5)$$

This is the supercurrent which flows uniformly between the two superconductors and is referred to as the Josephson supercurrent. In the eq. (1.5), I_0 is the maximum supercurrent that can flow through JJ and is known as the critical current. [8]

In a typical JJ experiment, we usually apply a current that flows through the JJ and then we measure the resulting output dc voltage. A commonly used electrical circuit model for measuring the voltage across the Josephson junction is called the Resistively and Capacitively Shunted Junction (RCSJ) model. This model assumes an equivalent circuit schematically depicted in fig. 1.2.

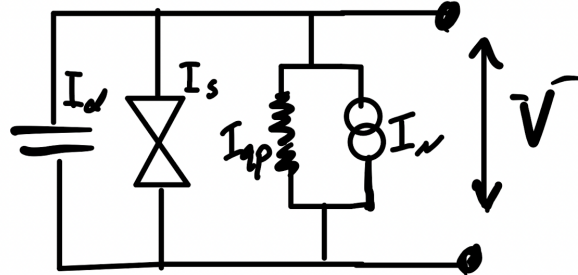


Figure 1.2: Schematic electronic equivalent circuit of JJ and a RCSJ.

According to Kirchhoff's law one can write the constant total current $I = I_d + I_{qp} + I_s + I_n$ ⁴, which is coming from the current source divides into four components, (I) the supercurrent $I_s = I_0 \sin [\varphi(t)]$;

³Here by gauge invariant phase we mean, e.g., that the expression $\vec{\nabla} \varphi(t, \mathbf{x})$ will remain unchanged under using gauge transformations, that is, if we transform $\varphi_0(t, \mathbf{x}) \rightarrow \varphi_0(t, \mathbf{x}) + \frac{q_s}{\hbar} \chi(\mathbf{x})$ and $\vec{A}(t, \mathbf{x}) \rightarrow \vec{A}(t, \mathbf{x}) + \vec{\nabla} \chi(\mathbf{x})$, where $\chi(\mathbf{x})$ is any scalar field, we would see that the phase and subsequently supercurrent density will be invariant under these transformations. For more detail see the Ginzburg–Landau theory. [7]

⁴This constant current arises from the conservation law of net charge in the components.

- (II)** dissipative (quasiparticle) current at normal electrodes $I_{qp} = \frac{V}{R_N}$; where R_N is a resistor at the barrier;
- (III)** displacement current $I_D = C_J \dot{V}$; where C_J is a capacitance across junction;
- (IV)** At finite temperature T , the resistance simultaneously generates a thermal noise, which is represented by Johnson–Nyquist noise current source I_n parallel to the R in the fig. 1.2. It refers to the random fluctuations with Gaussian distribution that arise due to the thermal energy and agitation of electrons in the resistances. Here the current source in shunt is given by $i_n = \sqrt{\frac{4k_B T \Delta f}{R}}$, where Δf is the bandwidth in hertz over which the noise is measured. We will investigate it experimentally later on in Chapter 4.

By neglecting the thermal noise sources in fig. 1.2

$$I = I_0 \sin [\varphi(t)] + \frac{V(t)}{R_N} + C_J \frac{dV(t)}{dt}, \quad (1.6)$$

which can be rewritten using eq. (1.4) via Josephson phase, φ instead of V as

$$I = I_0 \sin (\varphi) + \frac{1}{R_N} \frac{\Phi_0}{2\pi} \dot{\varphi} + C_J \frac{\Phi_0}{2\pi} \ddot{\varphi}. \quad (1.7)$$

One can also derive the eq. (1.7) as the equation of motion (EoM) of a particle with coordinate φ moving in a potential energy $U(\varphi)$, using the Euler–Lagrange equation. The Josephson potential energy $U(\varphi)$ can be written as a cosinusoidal function

$$U(\varphi) \equiv E_j(1 - \cos \varphi - \gamma \varphi), \quad (1.8)$$

where $\gamma \equiv I/I_0$ represents the normalized bias current, and $E_j \equiv I_0 \Phi_0 / 2\pi$ is the so-called Josephson coupling energy. Fig. 1.3 illustrates the Josephson potential for different values of the γ . We observe that when $\gamma = 0$, the potential is mirror-symmetric (purple curve), and as γ increases, the potential becomes tilted. The shape of $U(\varphi)$ resembles an old-fashioned washboard, thus it is referred to as a tilted washboard potential. It is evident that the tilt of the potential arises from γ . Specifically, the particle’s phase motion on the purple, green, and red curves, where $0 \leq \gamma < 1$ exhibits periodic oscillation. On the blue curve with $\gamma \geq 1$, however, the particle does not exhibit periodic oscillation [9].

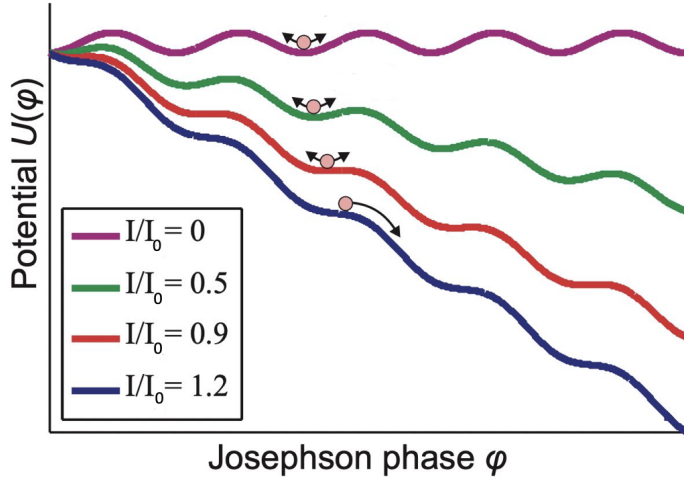


Figure 1.3: Plots of the tilted washboard potential $U(\varphi)$ are shown for several values of the tilt (bias current) γ . When $\gamma < 1$, the phase particle is trapped in the minimum of the potential. However, when $\gamma \geq 1$, the particle escapes from the minimum and slides down the potential.

It is often practical to use normalized units, therefore we introduce a new normalized time $\tau \equiv \frac{t}{\tau_c} = \frac{t}{2\pi e I_0 R} \Phi_0$. So that eq. (1.7) becomes

$$-\gamma + \sin [\varphi(\tau)] + \frac{d\varphi}{d\tau} + \beta_c \frac{d^2\varphi}{d\tau^2} = 0, \quad (1.9)$$

where $\beta_c \equiv \frac{\omega_c^2}{\omega_p^2} = \frac{2\pi}{\Phi_0} I_0 R_N^2 C$ is so called Stewart-McCumber parameter.

1.2 Current Voltage Characteristic (IVC)

Now let us see how a dc current-voltage characteristic (IVC) of the JJ looks like. In an experiment, we typically apply different values of dc currents I and measure an average (dc) voltage across the junctions for each current value of I , denoted as $\bar{V}(I)$. Using the known periodic phase evolution $\varphi(t)$, which can be obtained by solving the eq. (1.9) for $\varphi(t)$, the average voltage can be calculated as follows

$$\bar{V}(I) = \frac{1}{T} \int_0^T V(t) dt \stackrel{(1.4)}{=} \frac{1}{T} \int_0^T \frac{\Phi_0}{2\pi} \frac{d\varphi}{dt} dt = \frac{1}{T} \frac{\Phi_0}{2\pi} \overbrace{[\varphi(T) - \varphi(0)]}^{2\pi} = \frac{\Phi_0}{T}, \quad (1.10)$$

where we use 2nd Josephson equation in the second equality. The parameter $T = \frac{2\pi}{\omega}$ represents the time it takes for a particle to complete one period of the potential shown in fig. 1.3. Eq. (1.9) and (1.10) together can be used to obtain the typical IVC for different values of β_c as shown in fig. 1.4

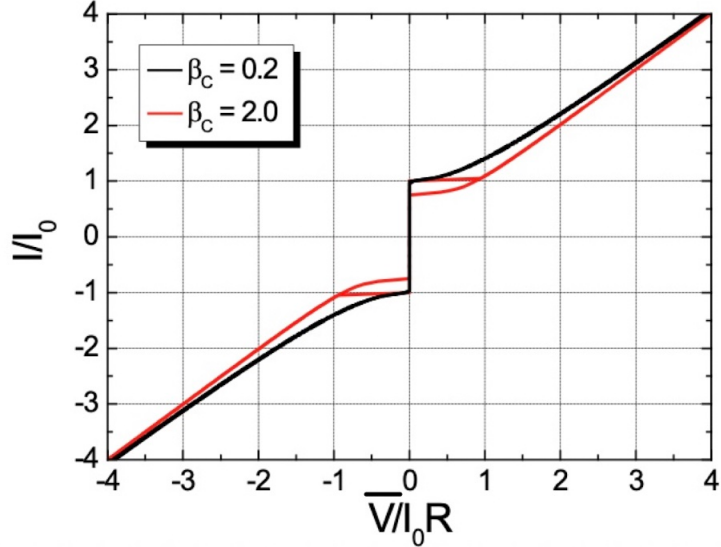


Figure 1.4: Current-Voltage Characteristic (IVC) of a symmetric potential.

For $\beta_c \ll 1$, where friction term $\dot{\varphi}$ dominates, one can neglect the last term ($\beta_c \ddot{\varphi}$) in the eq. (1.9). This leads to a non-hysteretic IVC, represented by the black curve in fig. 1.4. In this case, one can determine the time it takes for the particle to complete one period of the tilted potential as $T = \frac{2\pi\tau_c}{\sqrt{\gamma^2 - 1}}$ and calculate the averaged voltage,

$$\bar{V} = \begin{cases} I_0 R \sqrt{\gamma^2 - 1} & \text{if } \gamma > 1, \\ -I_0 R \sqrt{\gamma^2 - 1} & \text{if } \gamma < -1, \\ 0 & \text{otherwise.} \end{cases} \quad (1.11)$$

For $\beta_c \gg 1$, the inertia term $\ddot{\varphi}$ in eq. (1.9) becomes dominant, resulting in a hysteretic IVC (the red curve in the Fig. 1.4). In this case, one can investigate how the thermal fluctuation noise can characterize and adjust the hysteresis observed in the red curve shown in fig. 1.4. This can be achieved by incorporating $I_n(t)/I_0$ into the γ term in the potential eq. (1.8). The characterization of this effect can be quantified through a thermal noise parameter defined as [9]

$$\Gamma \equiv \frac{K_B T}{E_j} = \frac{2\pi K_B T}{I_0 \Phi_0} = \frac{I_{\text{th}}}{I_0}.$$

To this end, we would like to highlight that the IVC is completely symmetric. In other words, $\bar{V}(I) = -\bar{V}(-I)$. [9]

1.3 Josephson Junction in a Magnetic Field

In the following, we will study the dependence of the IVC on the externally applied magnetic field, denoted as H , to the JJ. Specifically, we are interested in the dependence of $I(H)$. Firstly, we will determine how magnetic field affects the gauge invariant phase differences across the barrier JJ. Then, we will incorporate the phase differences across the JJ $\varphi(t, \mathbf{x})$ into the definition of the supercurrent density $j_s(\varphi)$. Finally we will integrate it over the area of JJ to obtain the total supercurrent over the junction, denoted as $I_s(H) = \int_{S_j} j_s(\varphi) dA$. This $I_s(H)$ may take a range of values. Our objective is to determine the minimum or maximum value corresponding to I_c . In [9], the author considers a JJ with a rectangular geometry for simplicity and demonstrates how the applied magnetic field induces a gradient of phase differences φ , as given by

$$\frac{d\varphi}{dx} = \frac{2\pi}{\Phi_0} Bd_{\text{eff}}, \quad (1.12)$$

where $d_{\text{eff}} = d + 2\lambda \tanh(d/\lambda)$ is the effective magnetic thickness of the JJ, d is the thickness of BJJ, and λ is the London penetration depth. Without loss of generality, we assume a homogeneous and uniform applied magnetic field, denoted as $B(t, \mathbf{x}) \equiv B(x)$, which is applied along y -direction, $B(x) \equiv B_y(x)\hat{y}$, and is perpendicular to the JJ plane, defined by the (x, z) coordinates. Additionally, we observe that by the Ampère–Maxwell equation, we have $\vec{\nabla} \times B_y = \frac{\partial B_y(x)}{\partial x}\hat{z} = \mu_0 j_z(x)$. By taking derivative of eq. (1.12) with respect to x and using the Ampère–Maxwell equation, we obtain

$$\frac{\partial^2 \varphi(\mathbf{x})}{\partial x^2} = \frac{2\pi}{\Phi_0} d_{\text{eff}} \frac{\partial B_y(\mathbf{x})}{\partial x} = \frac{1}{\lambda_j^2} \frac{j_z(\mathbf{x})}{j_0} = \frac{1}{\lambda_j^2} \sin \varphi(\mathbf{x}), \quad (1.13)$$

where λ_j is so called the Josephson penetration depth⁵, which is defined as follows

$$\lambda_j \equiv \left(\frac{\Phi_0}{2\pi\mu_0 d_{\text{eff}} j_0} \right)^{1/2}. \quad (1.14)$$

We notice that for small applied magnetic field we can use Taylor expansion ($\sin \varphi \approx \varphi$) and solve eq. (1.13) to obtain $\varphi(x) = \varphi(0)e^{-x/\lambda_j}$. Now if we assume that our junction has length L smaller than Josephson penetration depth λ_j , then B_y fully penetrates into the JJ and becomes constant i.e., $B(x) \approx \text{const}$. Therefore, we consider a uniform magnetic field, which is homogeneously penetrates into the JJ and allows us to take the integral of eq. (1.12) by pulling B out of the integral and obtain

$$\varphi(t, \mathbf{x}) = \varphi_0 + \frac{2\pi}{\Phi_0} Bd_{\text{eff}}x. \quad (1.15)$$

⁵Notice that this calculation of λ_j is only valid for thick electrode e.g., $x > \lambda$. In the λ_j stays inductance which is equal to $\mu_0 d_{\text{eff}}$ only if $d_{\text{eff}} = 2\lambda$.

Hence one can rewrite the eq. (1.5) as follows

$$I(\mathbf{x}) = \int_{S_J} j_c(\mathbf{x}) \sin(\varphi(t, \mathbf{x})) d\mathbf{x}, \quad (1.16)$$

where $j_c(\mathbf{x})$ is a critical current density, which can be uniformly (e.g., $j_c(\mathbf{x}) = \text{const}$) or non-uniformly (e.g., $j_c(x, y)$) distributed. Therefore, the critical current density can be achieved by selecting a specific geometry and considering the presence of a magnetic field. The behavior of the supercurrent is investigated in [8] for various choices of current density and geometry. One can rewrite eq. (1.16) for a rectangular geometry of a BJJ (e.g., for a JJ with length $|x| \leq L/2$ and width W) as

$$I(x) = W \int_{-L/2}^{L/2} j_c(x) \sin(\varphi) dx = W \operatorname{Im} \left\{ e^{i\varphi_0} \int_{-L/2}^{L/2} j_c(x) e^{i2\pi Bd_{\text{eff}}x/\Phi_0} dx \right\}. \quad (1.17)$$

To obtain the maximum supercurrent, the eq. (1.17) should be maximized with respect to φ_0 , $\left| \frac{dI}{d\varphi_0} = 0 \right|$. We obtain

$$I = W \left| \int_{-L/2}^{L/2} j_c(x) e^{i2\pi Bd_{\text{eff}}x/\Phi_0} dx \right|. \quad (1.18)$$

This is the maximum Josephson current at any given applied magnetic field, H . Now if we assume a uniform critical current distribution i.e., $j_c(x) = \text{const}$ inside the JJ, then the eq. (1.18) yields the well-known Fraunhofer dependence.

$$I_c(\Phi_J/\Phi_0) = I_0 \cdot \left| \frac{\sin\left(\pi \frac{\Phi_J}{\Phi_0}\right)}{\pi \frac{\Phi_J}{\Phi_0}} \right| = I_0 \cdot \left| \operatorname{sinc}\left(\pi \frac{\Phi_J}{\Phi_0}\right) \right|, \quad (1.19)$$

where $\Phi_J = Bd_{\text{eff}}L$ is the total magnetic flux inside the junction and $I_0 = j_c \times S_J = j_c \cdot W \cdot L$. Eq. (1.19) can be rewritten for all values of Φ_J as

$$I_c\left(\pm(\Phi_J/\Phi_0)\right) = \pm I_0 \cdot \left(\operatorname{sinc}\left(\pi \frac{\Phi_J}{\Phi_0}\right) \right),$$

which can be plotted as shown in fig. 1.5. The signs also indicate maximum (I_{c+}) and minimum (I_{c-}) critical currents.

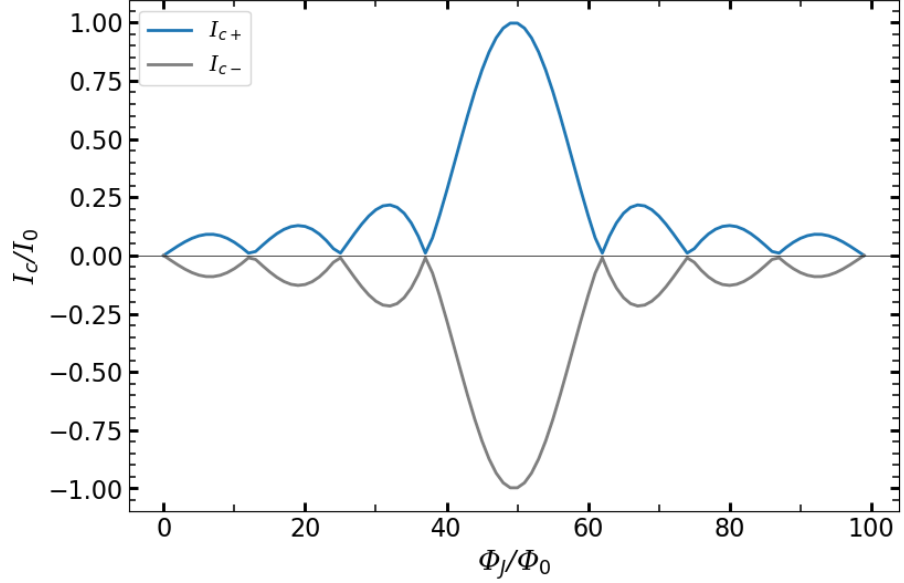


Figure 1.5: Negative and positive $I_c(\Phi_J)$ are symmetric for a fixed Φ_J . For example, when the value of Φ_J/Φ_0 is fixed at 44.5, we observe, $|I_{c+}/I_0| = |I_{c-}/I_0| = 0.75$.

Finally, we would like to point out that the $I_c\left(\pm(\Phi_J/\Phi_0)\right)$ values are symmetric with respect to the current polarity. In other words, for any fixed value of the flux Φ_J we find that $|I_{c+}| = |I_{c-}|$. [8]

Chapter 2

Theory of Ratchet

2.1 An Overview of Josephson Ratchet

When discussing a ratchet, the simplest model we have in mind is a periodic asymmetric potential¹ where a particle moves under the action of stochastic force with zero time averaged, as shown in fig. 2.1 (a). Such a force pushes the particle back and forth, but on average, the force does not push the particle anywhere forward or backward. However, due to the asymmetry of the potential, in some cases, one can observe a net transport in a particular direction. Consequently, the random force with zero time average can be transformed into directed particle motion, enabling the particle to perform useful work. We will delve further into this concept in the subsequent sections of this chapter.

Since we will consider Josephson system in this thesis, the particle will move in the potential along the coordinate φ . Therefore, the averaged velocity $\langle \dot{\varphi} \rangle$ of the particle, it is proportional to the averaged voltage, as described by eq. (1.4). Similarly, when we mention the application of current, as indicated in eq. (1.7), it is analogous to applying a force.². Hence, when we mention the application of a dc current to the system, it is synonymous with applying forces.

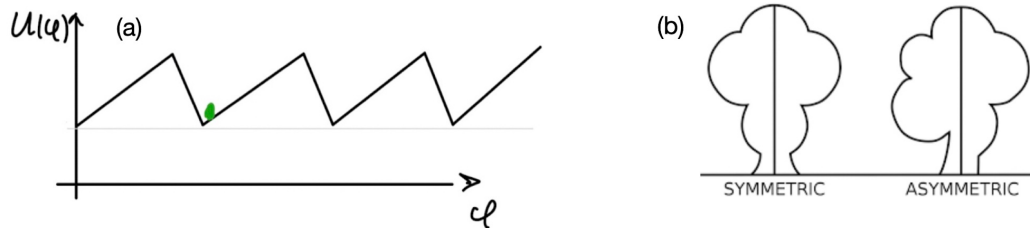


Figure 2.1: (a) An example of a particle trapped in a schematic asymmetric potential
(b) Schematically indicates the meaning of asymmetric.

¹by asymmetrical, we mean reflexion asymmetry, $U(-\varphi) \neq U(\varphi)$.

²The Newtonian force for a stationary potential can be written as $F = -\nabla_\varphi U(\varphi)$. Now if we use the Josephson potential eq. (1.8), we would get $F \propto \gamma$, which means that applied current is proportional to force.

So far, we have studied the symmetric Josephson potential in detail, as seen in eq. (1.8), and fig. 1.3. However to construct a Josephson ratchet, we need to design an asymmetric Josephson potential. We schematically show this kind of potential in fig. 2.1(a).

Similar to Chapter 1.1, in order to determine the IVC, one can derive the dependency of the averaged voltage on the current from an EoM analogous to eq. (1.9), but this time for an asymmetric Josephson potential instead of symmetric potential. A non-hysteretic IVC for asymmetric potential is schematically depicted in fig. 2.2.

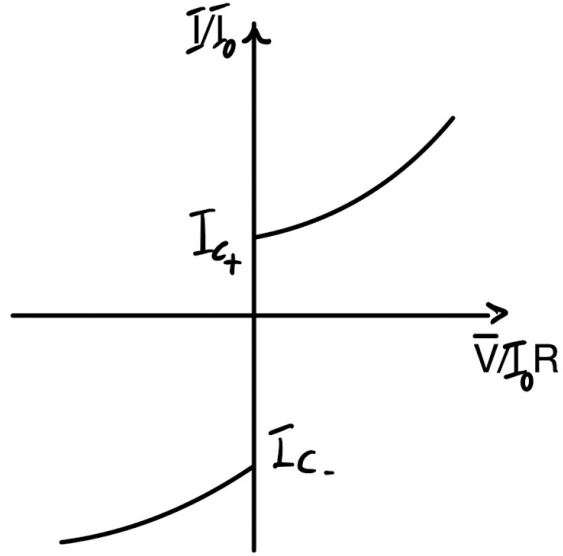


Figure 2.2: The schematic example shows an asymmetric non-hysteretic IVC for an asymmetric Josephson potential. I_{c+} represents the positive critical current, and I_{c-} represents the negative critical current.

We clearly observe that $|I_{c-}| \neq |I_{c+}|$, resulting in an asymmetric IVC, which is in contrast to what we obtained for the symmetric Josephson potential. This inequality in I_c values is attributed to the fact that in asymmetric potential, the maximum slopes of the potential in the left/right directions are different. Therefore, the force (applied current) needed to overcome this slope (critical current) is also different for each polarity. We can now quantify the degree of asymmetry by the asymmetry parameter \mathcal{A} . This parameter is generally defined as the ratio of the maximum slopes of the potential in the left and right directions

$$\mathcal{A} \equiv \frac{\max(|I_{c+}|, |I_{c-}|)}{\min(|I_{c+}|, |I_{c-}|)}. \quad (2.1)$$

Later, we will see that \mathcal{A} is one of the key parameters defining the performance of the ratchet.

2.1.1 Josephson Ratchet Operation

If the IVC exhibits a similar characteristic as shown in fig. 2.2, it is possible to operate a ratchet in the deterministic regime and construct a rectifier. Typically, a rectifier is achieved by applying an ac signal and obtaining a dc output signal. In our specific case, we apply an ac current and observe the ratchet effect through the response of the dc output. This effect can be accurately interpreted using a rectification curve $\langle V \rangle(I_{ac})$. Fig. 2.3 schematically illustrates this rectification curve.

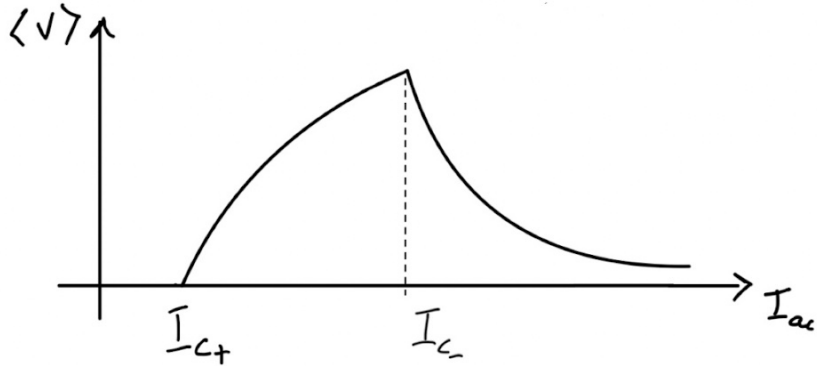


Figure 2.3: A rectification curve represents the average velocity of a particle ($\langle \dot{\phi} \rangle \propto V$) as a function of the applied ac-drive amplitude I_{ac} . The interval between I_{c+} and I_{c-} is called operation interval or the rectification window, which can be defined as $\Delta \equiv I_{c-} - I_{c+}$.

When an alternating current $I(t) = I_{ac} \sin(\omega t)$ is applied, it can be understood as tilting the potential back and forth at a frequency of ω . However, for small tilting amplitudes $I_{ac} < |I_{c_-}|$, we find that the particle remains trapped within the potential well, resulting in an average velocity (voltage) equaled to zero. For $I_{ac} > |I_{c_+}|$, the particle starts moving forward until it reaches its maximum average velocity at $I_{ac} \rightarrow |I_{c_-}|$. As I_{ac} is further increased, the average voltage gradually decreases until it eventually approaches zero. The range between I_{c_+} and I_{c_-} is known as the rectification window (RW), representing the interval during which the particle can move during a fraction of the positive and not move (remain trapped) during the negative semi-periods of the ac drive.

We observe that a larger asymmetry parameter results in a wider RW. In the absence of asymmetry (i.e., in the case of a symmetric Josephson potential with $\mathcal{A} = 1$ or $|I_{c_+}| = |I_{c_-}|$), the rectification curve (average velocity) remains zero, and the particle does not move in average. This occurs because the net average force exerted on the particle from both left and right sides of the symmetric potential well is zero. This can be seen, for example, in the purple curve depicted in fig. 1.3.

A relevant question arises: How good is a ratchet? How can we characterize its performance? Obviously, we want a ratchet to work not only for a certain amplitudes of the input signal, but for a very wide range of amplitudes, ideally from a small

amplitude to a very large amplitude. However, as we saw in fig. 2.3 the ratchet does not move for the small and very large amplitudes, and there is only a limited range of amplitudes (the RW), in which the rectification occurs ($\langle V \rangle \neq 0$). Therefore, to achieve a broad operational range for the ratchet, we aim to maximize the size of the RW. This entails minimizing $|I_{c+}|$ and maximizing $|I_{c-}|$. Consequently, a larger asymmetry parameter \mathcal{A} leads to an expanded interval of operation, enabling a wider range of amplitudes in which the ratchet can function effectively.

However, even if the ratchet is capable of rectification, it does not yet generate useful work or deliver rectified power to a load. We refer to such a ratchet as being idle. To prevent the ratchet from being idle, we should load it i.e., by applying counterforce, typically in the form of a dc current I_{dc} . This counterforce tilts the potential and pushes the particle in the opposite direction to the ratchet motion. If the ratchet effect is stronger than this counterforce, the particle will overcome the constant (counter) slope and ascend, thereby performing useful work. Fig. 2.4 schematically depicts a loaded ratchet.

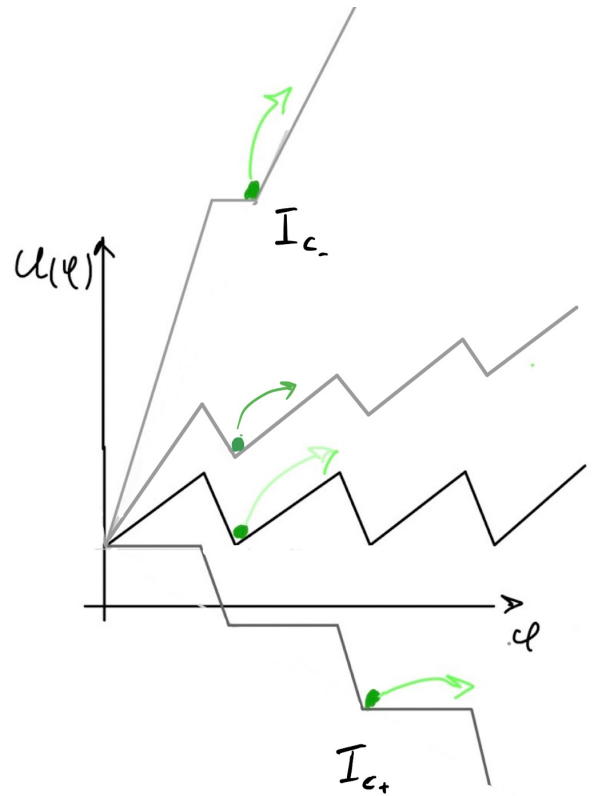


Figure 2.4: A ratchet potential for $I_{dc} = 0, I_{c-}, I_{c+}$.

If the countercurrent becomes too large, the ratchet stops. We refer to such a current as the stopping current or stopping force. As illustrated in fig. 2.4, if the ratchet transport initially occurs in the positive direction along the φ -axis, we apply $I_{dc} < 0$. This results in a potential tilt of $-I_{dc} \cdot \varphi$, allowing the particle can still climb due to the ratchet effect and perform some useful works.

The rectification curve for a loaded ratchet is schematically depicted in fig. 2.5.

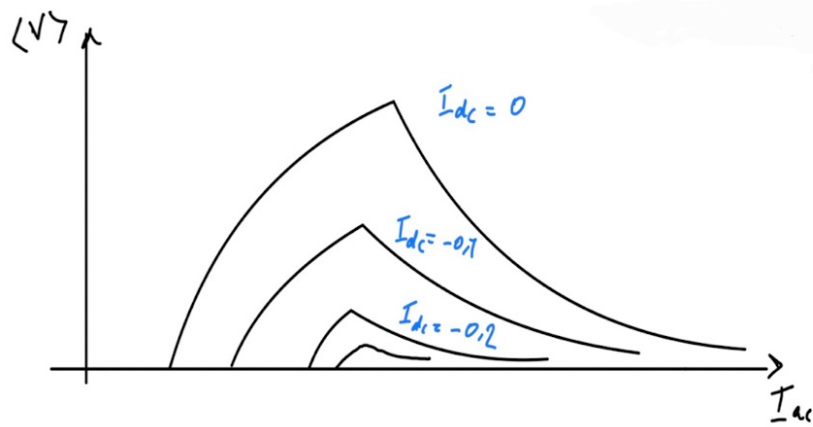


Figure 2.5: The schematic loaded ratchet up to countercurrent $|I_{dc}| = 0.2 \mu\text{A}$.

It is evident that gradually increasing the load $|I_{dc}|$ leads to a reduction in the size of the rectification window and the values of \bar{V}_{dc} . This reduction shows that the ratchet is not strong enough for any I_{ac} . Specifically, we observe that as the load $|I_{dc}|$ increases, the operational range in terms of I_{ac} decreases. However, in this narrower interval, the particle is compelled to move against the ratchet motion and produce more useful power. Our primary objective is to maximize both the rectification windows (RWs) and the value of the stopping current.

To summarize this section, let us consider an example simulation of a ratchet³ that was studied in [1] and [4]. The simulations were conducted in a quasistatic regime, allowing for the acquisition of information about the ratchet's operation solely from its asymmetric IVC. The authors generated a step-like asymmetric IVC, as shown in fig. 2.6(a), and simulated various figures of merit based on this asymmetric IVC. Fig. 2.6(b) presents the simulation results for a loaded rectification curve \bar{V}_{dc} .

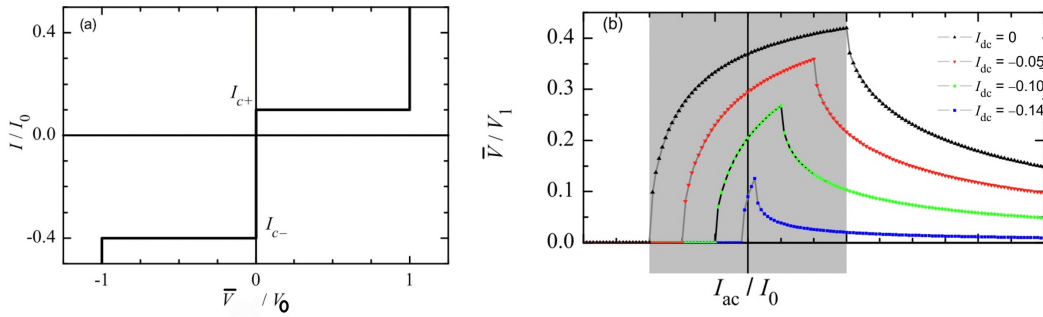


Figure 2.6: (a) A custom-made asymmetric IVC with $\mathcal{A} = 4$. (b) The rectification curves for several values of I_{dc} based on the asymmetric IVC, borrowed from [1].

³A deterministic underdamped Josephson vortex ratchet consisting of a long Josephson junction with $L \geq \lambda_j$.

The black curves in fig. 2.6(b) correspond to the case where $\mathcal{A} = 4$ and $I_{dc} = 0$. By loading the ratchet and increasing I_{dc} (colored curves), we observe that the rectification window (RW) becomes shorter. Consequently, the asymmetry parameter is reduced⁴. However, within this shorter interval, the particle can perform more useful work and achieve higher efficiency, as we will explain in the following subsection.

2.1.2 Efficiency

Efficiency is defined as useful output dc power \bar{P}_{out} divided by the total input power consumed by the system \bar{P}_{in}

$$\eta \equiv \frac{-\bar{P}_{\text{out}}}{\bar{P}_{\text{in}}}. \quad (2.2)$$

As a case study, the efficiency of the model investigated in [1] is presented in fig. 2.7(e). The black curve represents the idle ratchet, while the colored curves correspond to loaded ratchets with different values of $|I_{dc}|$. From fig. 2.7(c), we observe that as I_{ac} increases, the input power \bar{P}_{in} also increases, reaching its maximum at the end of the rectification window (RW). The ratchet operates with maximum efficiency η at the beginning of the RW for any stopping force, as shown in fig. 2.7(e). Furthermore, we notice that increasing $|I_{dc}|$ results in a shorter operation interval but a higher efficiency. In [4], it was demonstrated that the maximum efficiency achievable in principle is determined solely by the asymmetry of the potential, given by $\eta_{\max} = \frac{I_{c_-} - I_{c_+}}{I_{c_-} + I_{c_+}}$. Overall, we can observe that a higher asymmetry leads to a higher maximum efficiency.

⁴To see this, one can express the asymmetry parameter in terms of the rectification window as $\mathcal{A} = \frac{I_{c_+} + \Delta}{I_{c_+}}$, making it clear that decreasing Δ leads to a reduction in asymmetry.

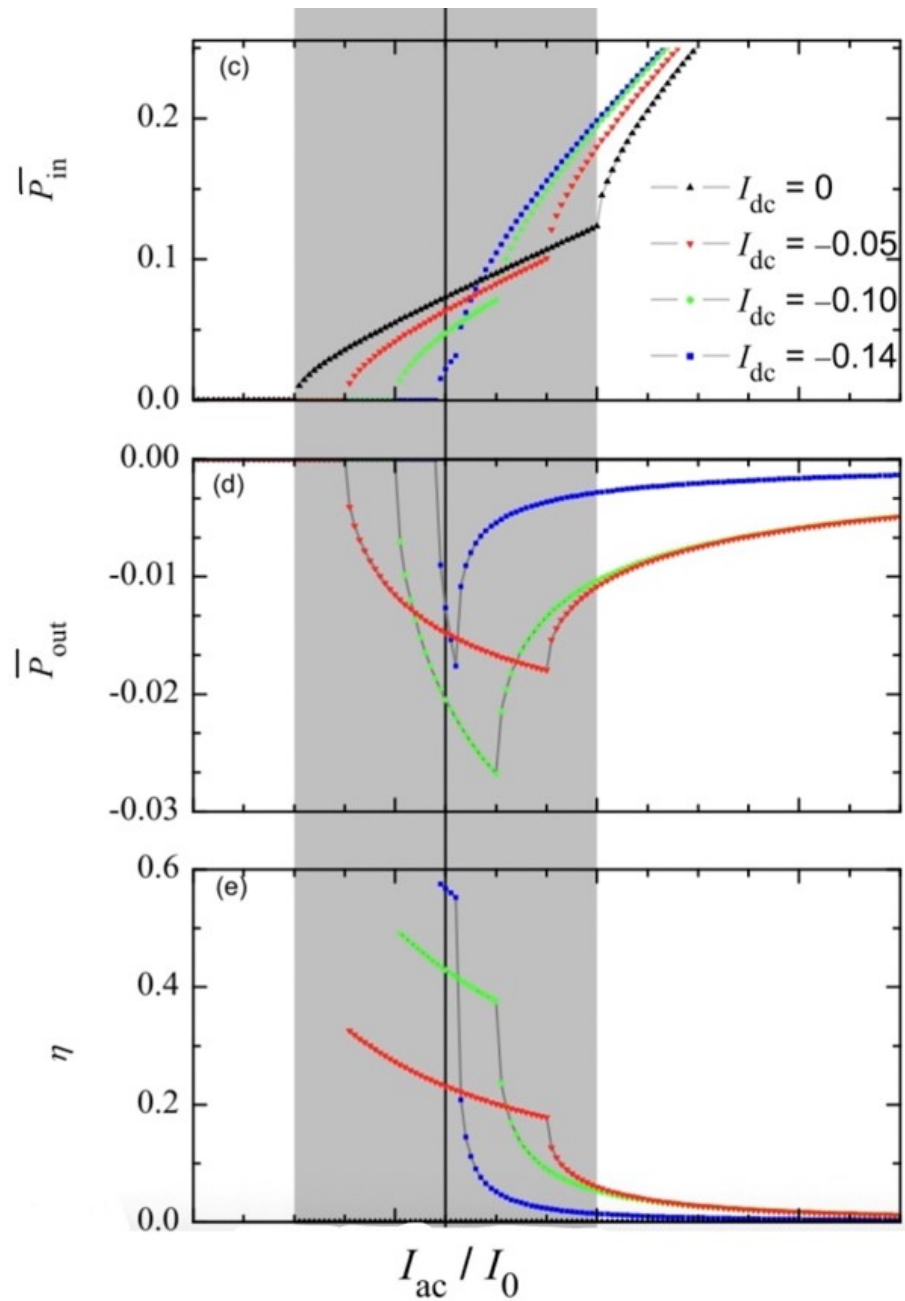


Figure 2.7: (c) Average input ac power \bar{P}_{in} , (d) average output dc power \bar{P}_{out} , (e) efficiency η , fig(4) of [1].

2.1.3 Junctions of In-line Geometry

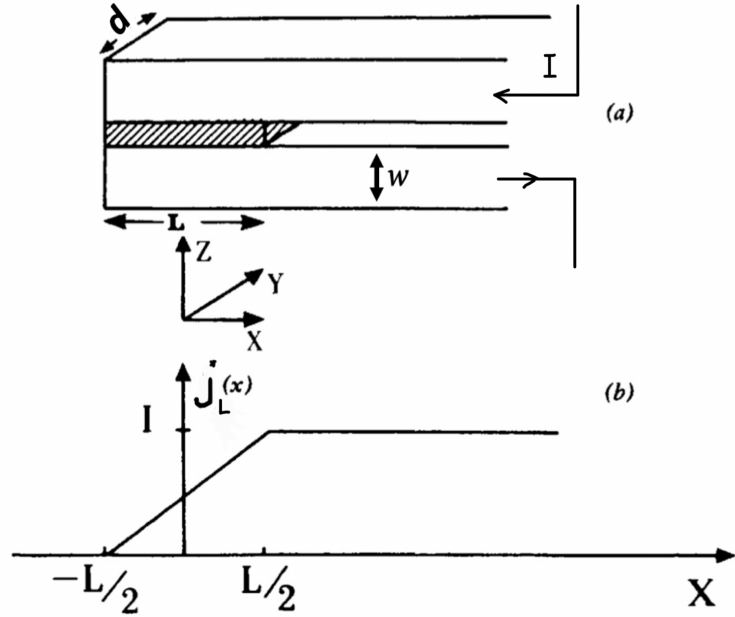


Figure 2.8: (a) The in-line geometry of a (JJ) consists of superconducting where the dashed line represents the barrier JJ surrounded by superconductors. The arrows indicate the current I flowing through the superconductors. (b) The current density j_L as a function of distance x .

In the classical textbook on the Josephson effect [8], Barone *et al.* considered an in-line JJ geometry, as shown in fig. 2.8(a). In this geometry, the bias current fed from the right side flows through the Josephson barrier (the dashed hatched region) and produces the so-called self-field. We assume that the maximum supercurrent corresponds to the uniform current flow across the Josephson barrier with the current density j_{c0} . By solving the continuity equation $\left(\partial_x\left(\frac{I_L}{d}\right) = j_{c0}\right)$ with the boundary conditions $I_L(-L/2) = 0$ and $I_L(L/2) = I_0$, we will obtain the current through the top electrode as

$$I_L(x) = j_{c0}d \left(x + \frac{L}{2} \right).$$

By solving Maxwell equation $\vec{\nabla} \times H_s = j_L(x)$, where $j_L(x) = I_L(x)/(wd)$, we obtain

$$H_s(x) = \frac{j_{c0}}{w} \left(\frac{x^2}{2} + \frac{Lx}{2} \right).$$

Following [8], we substitute this field profile by its average value

$$\bar{H}_s = \frac{5j_{c0}L^2}{12w} = \frac{5I_0L}{12wd}, \quad (2.3)$$

which represents the self-field when we apply the maximum supercurrent $I = I_0$ through the junction. If we apply arbitrary I , then the self-field will be given by $\bar{H}_s(I) = \bar{H}_s I / I_0$. The self-field together with the applied external magnetic field H_e , $H = H_e + H_s$ skews $I_c(H)$, as shown in fig. 2.9. The maximum Josephson current through Josephson junctions is given by (see eq. (5.1.4) of the book [8])

$$I(H_e) = dLj_{c0} \left| \frac{\sin \left(\frac{\mu_0 \pi d_{\text{eff}} L}{\Phi_0} H \right)}{\left(\frac{\mu_0 \pi d_{\text{eff}} L}{\Phi_0} H \right)} \right|, \quad (2.4)$$

for small junction compared to Josephson penetration depth. One can rewrite the eq. (2.4) in terms of normalized fluxes as follows

$$\frac{I_c(f)}{I_0} = \left| \frac{\sin \pi \left(f + f^M \frac{I_c(f)}{I_0} \right)}{\pi \left(f + f^M \frac{I_c(f)}{I_0} \right)} \right|, \quad (2.5)$$

where $I_0 = dLj_{c0}$ is the maximum value of supercurrent I . We have defined normalized flux $f \equiv \Phi_J/\Phi_0$, where $\Phi_J = d_{\text{eff}} L H_e$ is the total applied flux inside JJ. The length of the JJ is denoted by L , and the effective magnetic thickness d_{eff} is given by $d_{\text{eff}} = 2\lambda_{\text{eff}} \tanh(w/\lambda_{\text{eff}})$. Here, λ_{eff} is the effective London penetration depth, defined as $\lambda_{\text{eff}} = \lambda \coth(d/\lambda)$, where λ is the London penetration depth.

It is important to note that the Josephson penetration depth for the in-line geometry in this case differs from the eq. (1.14) in terms of magnetic thickness for the geometry shown in fig. 2.8. The Josephson penetration depth for the in-line geometry is defined as $\lambda_j \equiv \left(\frac{\Phi_0}{2\pi\mu_0 d' j_{c0}} \right)^{1/2}$, where $d'\mu_0$ is called specific inductance of electrode, and $d' = 2\lambda_{\text{eff}} \coth(w/\lambda_{\text{eff}})$ for our in-line geometry.

Additionally, we introduce $f^M \equiv \Phi_s^M / \Phi_0$ as the geometric normalized flux, where Φ_s^M describes the strength of the in-line geometry. It is determined by the eq. (2.4) and the definition of the self-field given in eq. (2.3)

$$\Phi_s^M = \mu_0 \bar{H}_s d_{\text{eff}} L = \frac{5\mu_0 L^2 d_{\text{eff}} I_0}{12dw}. \quad (2.6)$$

Φ_s^M describes how much the $I_c(H)$ plot is skewed and deviated from the symmetric dependence as shown in fig. 2.9. We can express f^M in terms of the Josephson penetration depth λ_j using the following equation

$$f^M = \frac{5L^3 d_{\text{eff}}}{24\pi\lambda_j^2 w d'}. \quad (2.7)$$

At $f^M = 0$, the maximum supercurrent $I_c(f)$ becomes unskewed and symmetric, following the Fraunhofer pattern $I(f) = I(-f)$ as given by the eq. (1.19) as shown

in fig. 1.5. Eq. (2.4) defines an implicit function of I on the flux f , which requires numerical solutions. We have developed a Python script that uses the bisection method to solve eq. (2.5) numerically. The script calculates $I_c(f)$ for several fixed values of f^M and is depicted in fig. 2.9. One can see the skewness of $I_c(f)$ depends on f^M . Visually, if we draw a vertical line at a fixed value of f , it becomes evident that $|I_{c+}| \neq |I_{c-}|$ for most of the f values. Therefore, we can quantify the degree of skewness using the asymmetry parameter \mathcal{A} .

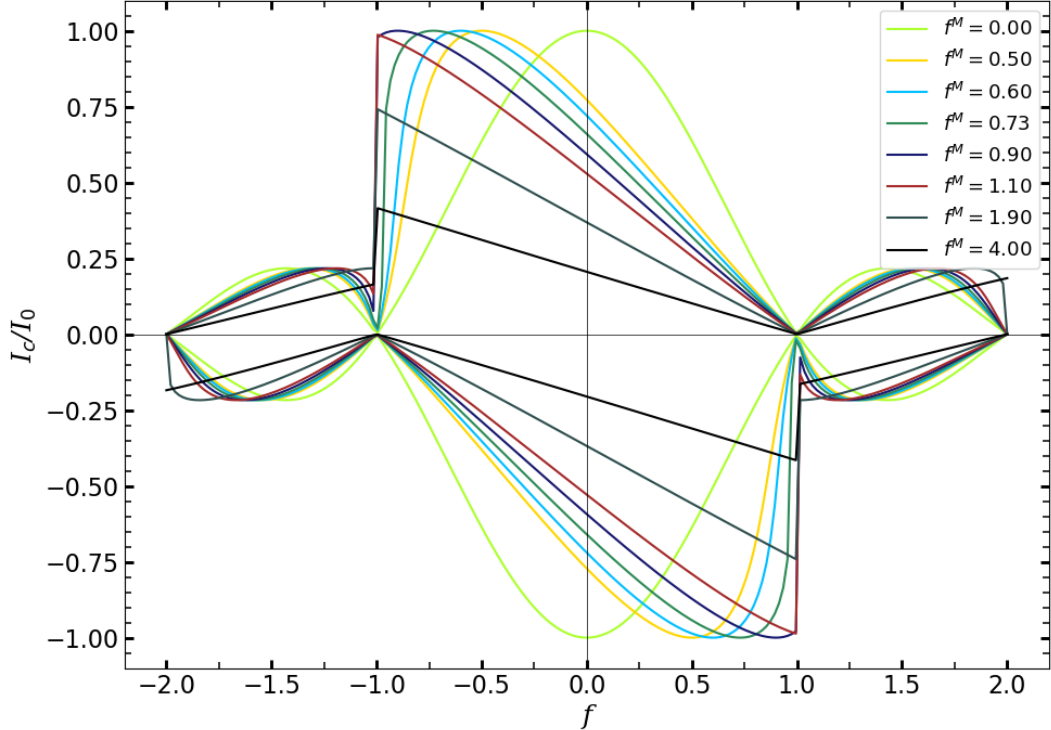


Figure 2.9: A family of asymmetric $I_c(f)$ for different f^M obtained by solving the eq. (2.4) numerically.

Note that the maximum asymmetry at the optimum point f_{opt} (where the asymmetry is maximum) of f is symmetric under changing the sign of f . Now let's examine the behavior of \mathcal{A} as a function of f for different values of f^M . In fig. 2.10(a), we can observe the dependence of the asymmetry parameter \mathcal{A} on f for various fixed values of f^M . For instance, for the blue curve ($f^M = 0.6$), we find that the asymmetry parameter $\mathcal{A} \approx 8$ at the optimum value of $f_{\text{opt}} \approx -0.9$. This maximum asymmetry value increases as the value of f^M increases. In fig. 2.10(b), we present the dependence of the maximum asymmetry $\mathcal{A}_{\text{max}}(f^M)$ at the optimum value of f . One can see from both fig. 2.10(a) and. 2.10(b) that \mathcal{A} increases with increasing f^M .

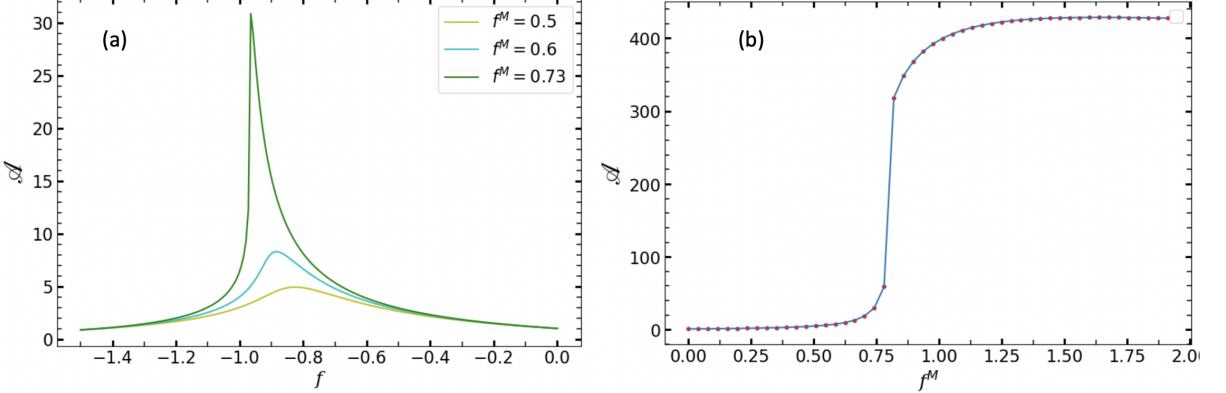


Figure 2.10: (a) Asymmetry parameter \mathcal{A} vs. magnetic flux f for different values of f^M (b) Asymmetry parameter \mathcal{A} vs. strength of in-line geometry f^M .

Thus, using in-line JJs and the appropriate applied normalized flux f , one is able to design a Josephson ratchet with a high asymmetry parameter. It is important to emphasize that the maximum asymmetry achieved at f_{opt} for the curve with a high value of f^M exceeds 100, as shown in fig. 2.10(b). This happens because from some optimum points (for example around $f^M \approx 0.9$) onward we observe that increasing the value of f^M does not alter the optimum point (see the fig. 2.9). Instead, one of the critical currents, specifically I_{c+} in our case, tends to approach zero at a faster rate compared to the other one (I_{c-}). Consequently, this leads to a divergence of the asymmetry parameter, approaching infinity as defined. However, it should be noted that achieving such high asymmetry in experiments is In reality, the system is subjected to substantial amounts of noise affecting the amplitude of $|I_{c\pm}|$, especially near the critical points, where $|I_{c\pm}|$ should approach zero. This substantial noise leads to a substantial reduction in the actual asymmetry parameter compared to the intended target parameter. Therefore, achieving extremely high asymmetry values as theoretically predicted is challenging in experimental settings.

In the next chapters, we will examine these challenges as well as the optimal target parameters for designing an effective Josephson ratchet. This will be done once we are prepared to commence the ratchet implementation.

Chapter 3

Fabrication and Implementation

3.1 Sample Information

The sample was prepared using commercial YBCO thin film produced by a company named Ceraco. The sample consists of a 2 inch LSAT substrate with 30 nm of $\text{YBa}_2\text{Cu}_3\text{O}_7$ (YBCO) film which is the thickness of insulator barrier JJ $d = 30 \text{ nm}$, and 20 nm of Au deposited on top. The detail information of the chip is provided by the company, as shown in fig. 3.1.

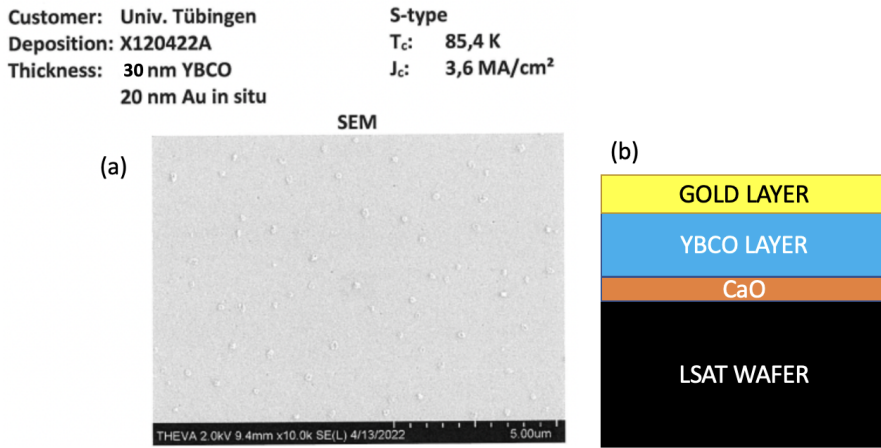


Figure 3.1: YBCO film on 2 inch LSAT substrate. (a) The scanning electron microscope picture of the sample surface. The critical temperature T_c and the value of the current density j_c are provided by Ceraco. (b) A schematic picture of the chip showing the deposition of its different layers.

3.2 Sample Layout

A $1 \times 1 \text{ cm}^2$ chip is divided into four similar smaller chips of $5 \times 5 \text{ mm}^2$. Each small chips is labeled with a letter: A, B, C and D. The layout of each small chip is shown in fig. 3.2. It consists of two columns of 18 bridges, making a total of 36 bridges.

Each bridge has two contact pads on one side, and all the bridges are connected to the main central lines (vertical in fig. 3.2), which is also connected to two ground pads on both sides.

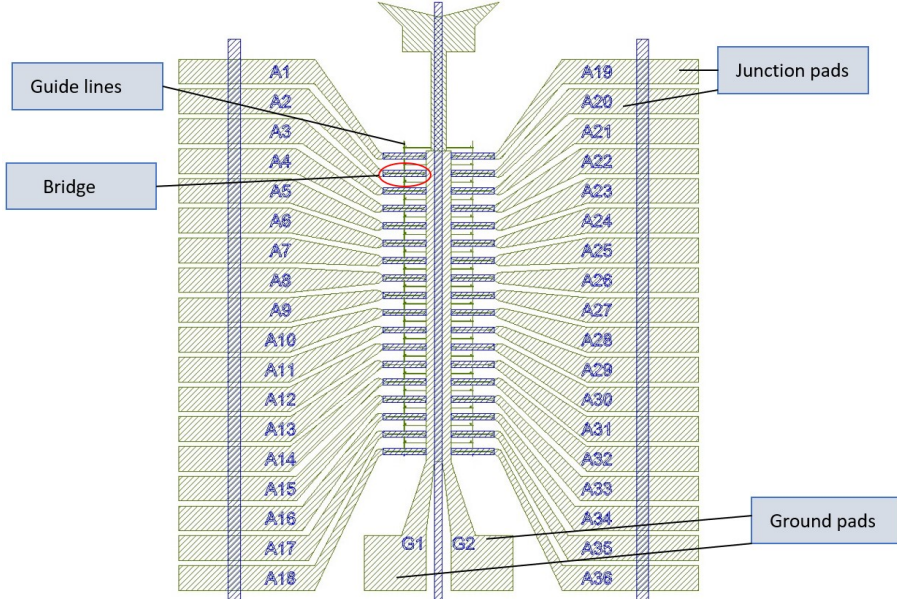


Figure 3.2: the layout of the small chip. The hatched light green areas correspond to the Au covered pads, while the blue areas represent the LSAT substrate. The guide lines are also covered by Au, and the Au layer is removed down to YBCO on the bridges.

3.3 Sample Fabrication

The first step of the fabrication process involves dicing the 2 inches film into four pieces of $5 \times 5 \text{ mm}^2$. These pieces are then cleaned using an ultrasound bath filled with acetone, followed by two rounds of cleaning with isopropanol in an ultrasound bath. After dicing and cleaning, the sample is spin-coated with a photoresist called “ma-P1205” and later dried on a hotplate at 90° Celsius for 210 seconds. The chip is then placed into a maskless aligner model for the patterning process, which consists of two steps.

(i). **Etching of the gold:** Once the chip is inside the maskless aligner, a laser beam scans the patterned layout as shown in fig. 3.3(a), which modifies the properties of the photoresist. The chip is then removed from the machine, and the modified photoresist is developed using “ma-D 331/S” for 50 seconds. It is quickly transferred to water to wash away the excess developer, and then transferred to another flask with water for further cleaning. The sample is then dried, and the gold is etched using an Argon ion beam. After the etching process is completed, the remaining photoresist is removed, and the chip is spin-coated again under the same mentioned conditions.

(ii). **Etching of the YBCO:** The chip is once again loaded into the maskless aligner to proceed with the second etching step. The same process as in step (i) is

carried out, but this time the machine scans another mask, as shown in fig. 3.3(b). The photoresist is modified again, and after removing the chip from the maskless aligner, it is selectively developed with “ma-D 331/S” and rinsed in water twice. Then, it is dried again, and the YBCO is etched with H₃PO₄ 0,1. After the etching process, the remaining photoresist is removed once again, and the chip is ready to be diced once more. Zoom-in pictures of the bridges after each step of etching are shown in fig. 3.4. [10]

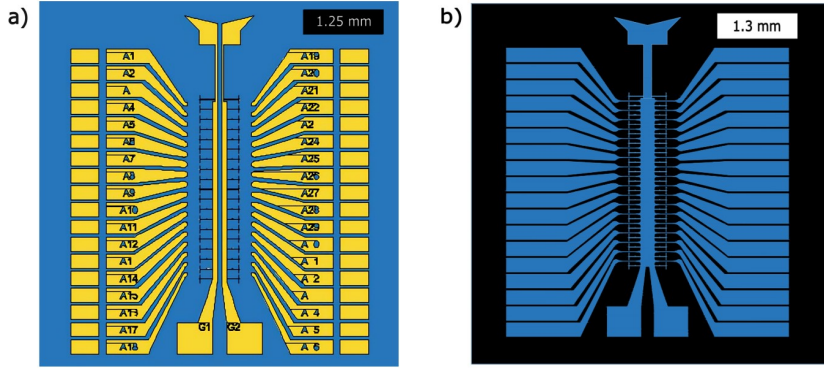


Figure 3.3: Masks used during the patterned process: (a) Mask used during step (i) for the etching of gold. The blue zone indicates where the gold has been removed, leaving only YBCO. The yellow zones indicate where the gold still remains. (b) The mask used during step (ii) for the etching of YBCO. The areas in blue represent the regions where the YBCO still remains. The black area represents LSAT (substrate). Note that in the regions where the gold remains from the first step (e.g., over the pads), it has not been removed during the second step.

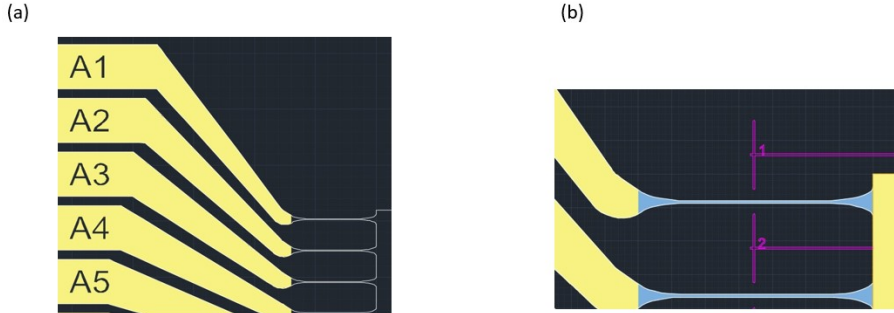


Figure 3.4: The microscope pictures of the sample after each step of the lithography process: (a) Picture of the pads after the step (i). The dark areas represent YBCO, and the yellow areas represent gold. (b) The picture of the bridges after the step (ii). The yellow area represents gold, the dark area represents LSAT, the blue area represents YBCO where the junction will be finally irradiated, and the purple lines are guide lines for our next step using He-FIB.

We are now ready to bring the sample to the Helium ion beam (He-FIB) to produce BJJ's and ratchets using the Focused Helium Ion Beam (He-FIB).

3.4 He-FIB

We utilize a He-FIB (Helium-Focused Ion Beam) system with an energy of 30 keV to fabricate the Josephson barrier and create the BJJ (Barrier Josephson Junction). The process is illustrated in fig. 3.5, which provides a concise overview of the He-FIB technique.

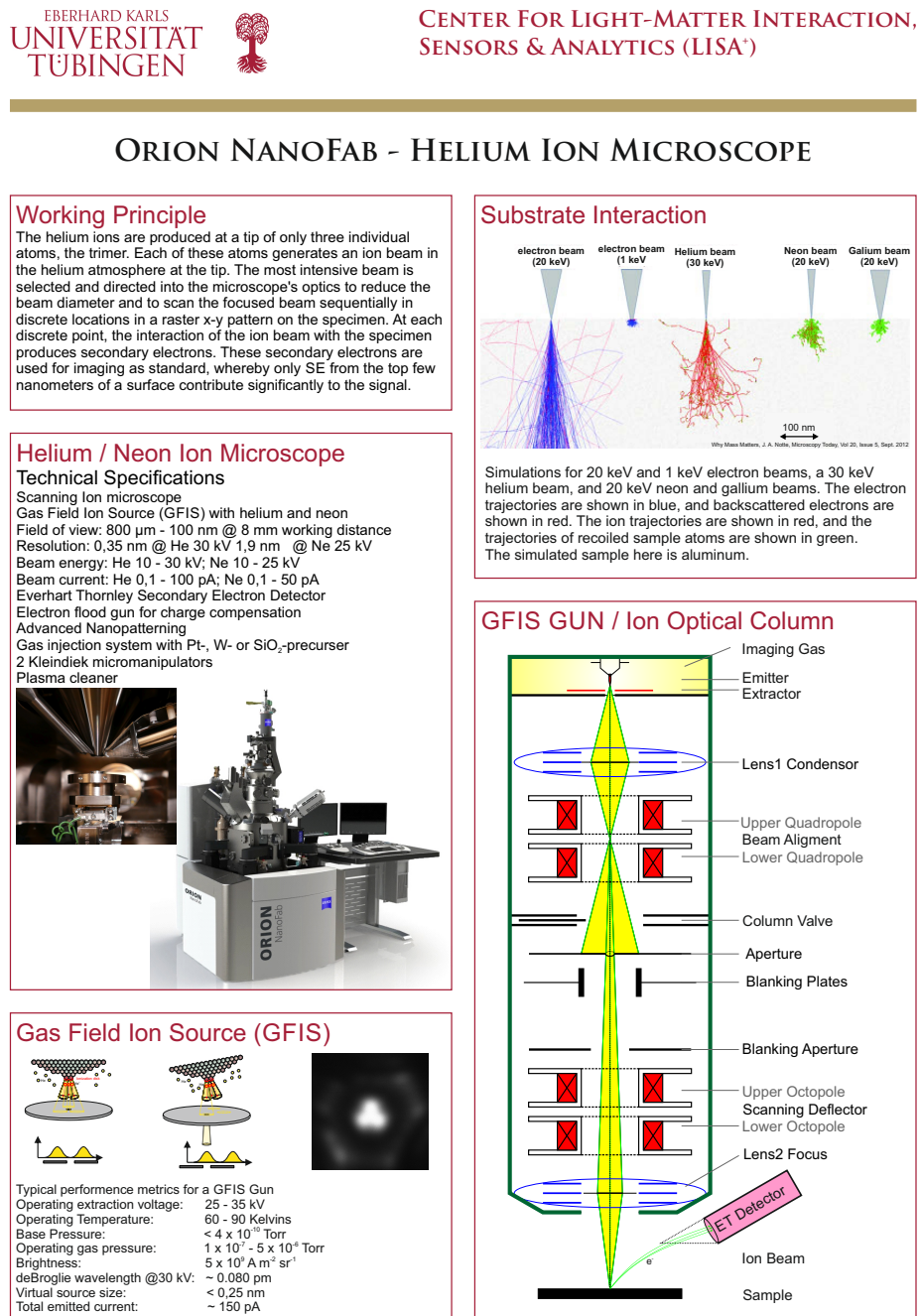


Figure 3.5: The poster of He-FIB.

The schematic illustration of producing BJJ using He-FIB is shown in the fig. 3.6.

We create the Josephson barrier depending on the Dose D by irradiating the bridge a long the line with a certain Dose (ionS/nm). The helium ions create either a very thin (few nm) amorphous region or a line (also a few nm wide) that suppresses I_c (changed doping), thus acting as the Josephson barrier between two superconductors (BJJs). In [11], it was experimentally shown that the critical current density j_c of the resulting BJJ depends on the irradiation dose D approximately as follows

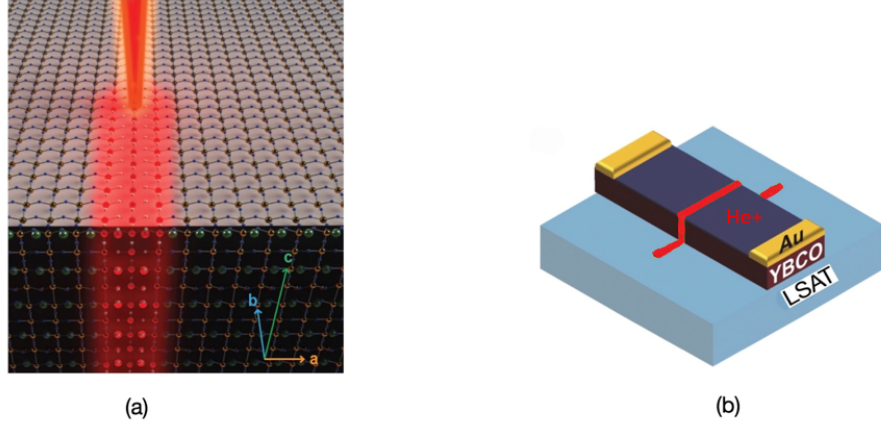


Figure 3.6: (a) The red line indicates focused He ion beam on the atomic level with a width of the order of a few nm. (b) Schematic sketch of the BJJ produced by He-FIB, where the red line indicates the barrier JJ.

$$j_c(D) \approx j_{c0} \exp(-D/D_0), \quad (3.1)$$

where j_{c0} (A/cm^2) and D_0 (ionS/nm) are the fitted critical current density at $D = 0$ and the characteristic dose, respectively, obtained by fitting experimental data using eq. (3.1).

The BJJs made by He-FIB can be changed continuously from a conducting to a completely insulating state by varying the irradiation dose. In fact, high-dose He-FIB irradiation disturbs the internal atomic structure of YBCO, making the irradiated line amorphous and highly resistive. It can effectively act as a resistive wall with $j_c = 0$. We utilize this technique to fabricate Josephson ratchets with more complex geometries than BJJs (see, for example, fig. 3.12).

3.5 Characterization

Before implementing the ratchet, we conducted a characterization of a series of BJJs with varying doses to determine the values of j_{c0} and D_0 for our specific chip. We fabricated 11 BJJs with dose series ranging between (450...700) ionS/nm and subsequently measured the critical current of each junction. The results are presented in table. 3.1

BJJs	Dose (ion/nm)	Maximum I_c (μA)
D19	455	15.6
D20	455	13.2
D21	505	11.5
D22	505	6.8
D23	556	1
D24	556	3.7
D25	606	1.4
D26	606	0.59
D27	657	0.17
D28	657	0.79
D29	707	0.29

Table 3.1: The maximum I_c is determined by measuring $I_c(H)$ and selecting the highest value, which may be reduced when $I_{\text{coil}} \neq 0$.

Next, we wrote a short python script to fit the experimental data using eq. (3.1) with j_{c0} and D_0 as fitting parameters. The result is shown in the fig. 3.7.

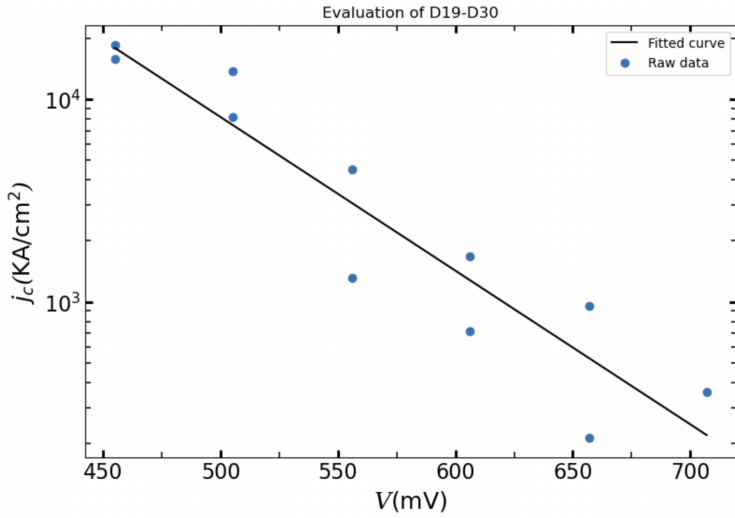


Figure 3.7: BJJs characterization of $j_c(D)$ experimental data and fit. 11 BJJs with the dose $D \approx 450\ldots700$ ionS/nm. The width of the BJJs is $W = 2.8\text{ }\mu\text{m}$ and the film thickness $d = 30\text{ nm}$.

As a result of fitting, we obtained $j_{c0} \approx 5\text{ kA}/\text{cm}^2$ and $D_0 = 57.2\text{ ionS}/\text{nm}$. As an example, we present IVC and $I_c(H)$ of several BJJs in fig. 3.8 to fig. 3.11.

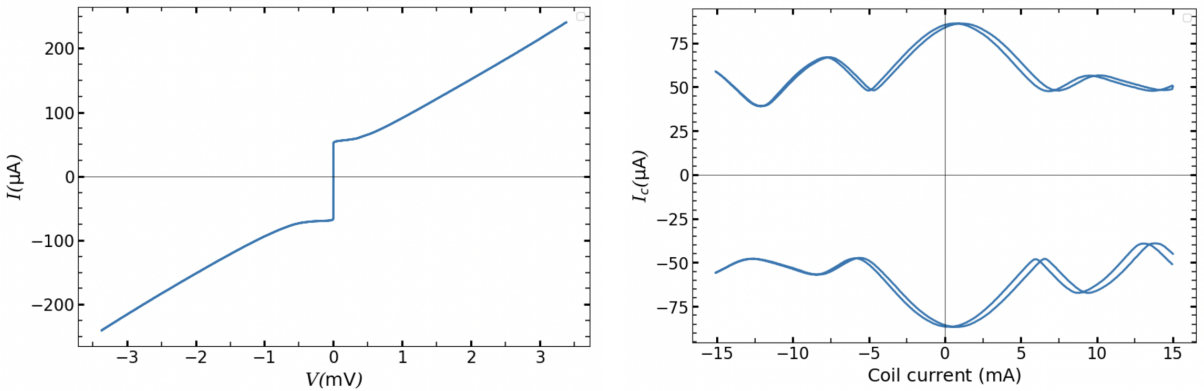


Figure 3.8: IVC and $I_c(H)$ of junction B28 with $D = 350 \text{ ionS/nm}$.

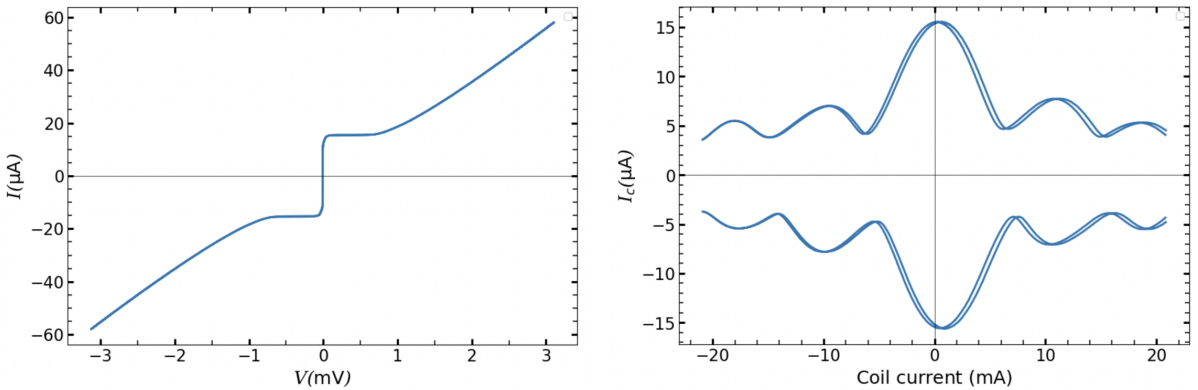


Figure 3.9: IVC and $I_c(H)$ of junction D19 with dose $D = 450 \text{ ionS/nm}$.

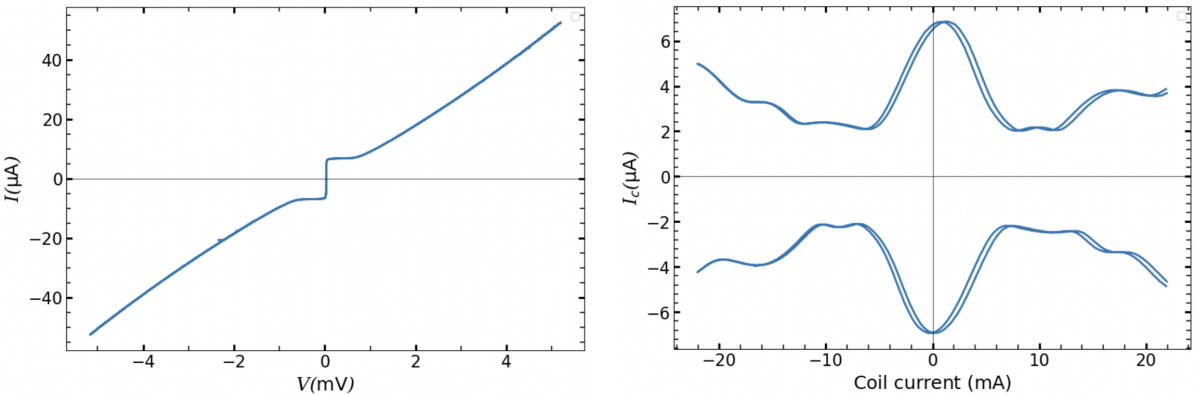


Figure 3.10: IVC and $I_c(H)$ of junction D22 with dose $D = 505 \text{ ionS/nm}$.

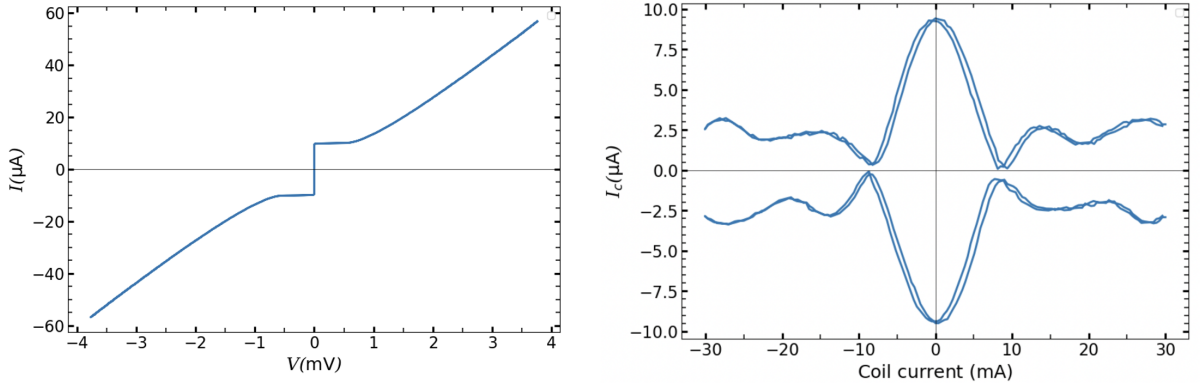


Figure 3.11: IVC and $I_c(H)$ of junction B33 with dose $D = 600 \text{ ionS/nm}$.

3.6 Implementation of an In-line Geometry Josephson Ratchet

In-line geometry

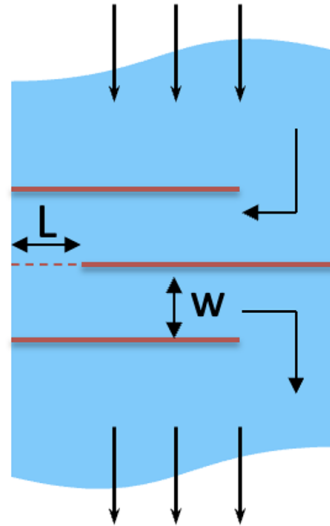


Figure 3.12: Sketch of the Josephson ratchet. The blue zone is YBCO, the red solid lines are the resistive walls, dash red line is the BJJ, and arrows indicate the flow of the supercurrent through the Josephson ratchet. w is the distance between two resistive walls and L is the length of BJJ.

In the Chapter 2.1.3, we explored the impact of the in-line geometry of a Josephson junction (JJ) on the generation of a self-field within our device. This field is characterized by f^M , which is described by the eq. (2.7). Additionally, we examined

how this parameter influences the skewness of $I_c(H)$ and, consequently, the asymmetry parameter.

In this master thesis we focus on the implementation of a highly efficient ratchet based on reasonable theoretical parameters. For instance, eq. (2.7) clearly demonstrates the geometric dependencies of the f^M on the length L of JJ and w . Therefore, we would design the ratchets with various values of f^M , while varying the length L of the JJ through definition of f^M in eq. (2.7).

To optimize the distance between the two resistive walls w , we must avoid making it too small (e.g., less than or equal to 100 nm) to prevent the destruction of the crystal configuration of YBCO due to the resistive walls. Moreover, extremely small values of w can lead to the emergence of topological defects. Throughout this work, we refrain from reducing w below 200 nm.

Hence, our target parameters are selected as follows: after determining the desired value of the dimensionless parameter f^M , we fix the supercurrent density $j_c(D)$ by adjusting the He-FIB irradiation dose using eq. (3.1). From the value of j_c , we calculate the Josephson penetration depth λ_j and determine the appropriate length L using eq. (2.7). Knowing j_c we can find the critical current by $I_c = j_c \cdot L \cdot d$, where in our case, $d = 30$ nm. It is important to mention that the expression for the Josephson penetration depth given by λ_j can be recalculated to show the effect of the inductance of superconductor electrode explicitly as

$$\lambda_j^K = \sqrt{\frac{\Phi_0 L}{2\pi j_c 2L_K d}}, \quad (3.2)$$

where $L_K = \mu_0 \lambda^2 \frac{L}{w \cdot d}$ is the kinetic inductance. Substituting L_K into the eq. (3.2) gives us

$$\lambda_j^K = \sqrt{\frac{\Phi_0 w}{4\pi \mu_0 j_c \lambda^2}}.$$

Next, similar to the Chapter 2.1.3, we can write f_K^M with respect to the λ_j^K as

$$f_K^M = \frac{5L^3 d_{\text{eff}}}{24\pi(\lambda_j^K)^2 w d'},$$

where $d' = 2\lambda \coth(w/\lambda)$ ¹.

In the table. 3.2, we present two sets of target parameters for the ratchets A15 and A22, which will be discussed in detail later.

¹Notice that, to explore this inductance effect further in detail for our geometry, it is necessary to formulate the sine-Gordon equation for the Josephson ratchet.

Target Parameters	A15	A22
$w(\text{nm})$	300	200
Dose(ionS/nm)	507	531
$j_c (\text{kA}/\text{cm}^2)$	7.15	4.8
$I_c (\mu\text{A})$	3.8	2.5
$\lambda_j(\text{nm})$	250	250
$L(\text{nm})$	1750	1750
$l \equiv L/\lambda_j$	7	7
f^M	0.25	0.26
$\lambda_j^K(\text{nm})$	2960	2960
$l_K \equiv L/\lambda_j^K$	0.6	0.6
f_K^M	0.09	0.1

Table 3.2: Comparison table of target parameters between ratchet A15 and A22.

Chapter 4

Experimental Results

4.1 An Overview

In this chapter, we report the set of experimental results for the ratchets A22 and A15. First we compare the actual (experimental) and target (theoretical) parameters of each devices, then we will present our experimental data for the set of measurements, including IVC, $I_c(H)$, \bar{V}_{dc} , \bar{P}_{out} , \bar{P}_{in} , and finally, the efficiency η . We will then compare our experimental results with the figures of merit of our ratchets, which are simulated in the quasistatic regime. Finally, we will drive our system with stochastic drive (Gaussian drive) and investigate the effect of different type of noises such as external and internal noises. It is shown how the noises due to some internal noise e.g., thermal sources can be rectified into the output dc voltage.

4.2 Josephson Ratchet A22

In the table. 4.1, the actual and target parameters of the device A22 are presented.

A22	Target parameter	Actual parameter
$w(\text{nm})$	200	200
Dose(ionS/nm)	531	531
$j_c (\text{kA}/\text{cm}^2)$	4.8	28
$I_c(\mu\text{A})$	2.5	14.8
$\lambda_j(\text{nm})$	250	103
$L(\text{nm})$	1750	1750
$l_j \equiv L/\lambda_j$	7	17
f^M	0.26	1.54
$\lambda_j^K(\text{nm})$	2960	1220
$l_K \equiv L/\lambda_j^K$	0.6	1.4
f_K^M	0.1	0.63

Table 4.1: Comparison table of target and actual parameters of ratchet A22. Notice that we chose $\lambda = 250 \text{ nm}$ and subsequently $\lambda_{\text{eff}} = 2 \mu\text{m}$.

In general, discrepancies between the actual and target parameters can arise due to various factors such as fabrication techniques, lithography processes, and the accuracy of I_c measurement. The dose D has a fairly precise accuracy of around two percent. Since the precision of He-FIB is on the scale of a few nanometers, our geometric parameters such as length L and w align exactly with the planned specifications. By eq. (3.1) we saw that j_c has exponential dependence on dose and the spread is quite high, which is typical for our technology. Consequently, I_c , λ_j , the normalized length l_j , and f^M will follow from their definitions and dependencies on j_c . (

The IVC of the ratchet A22 is presented in the fig. 4.1 as follows

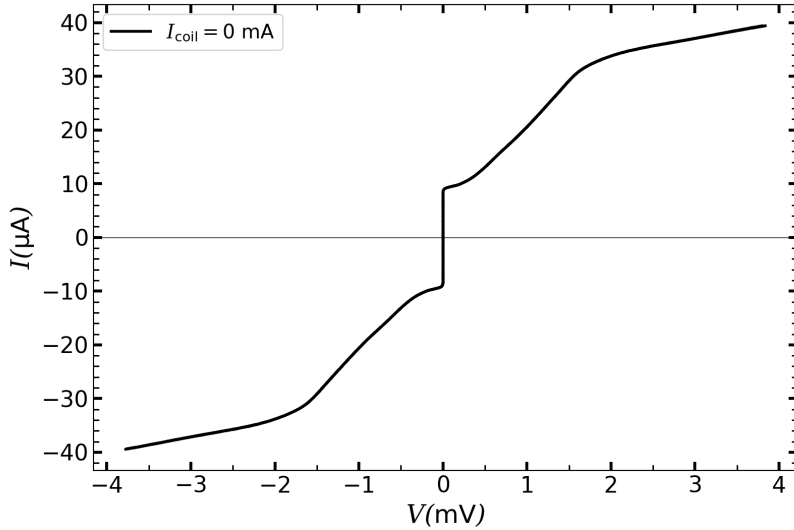


Figure 4.1: IVC of the ratchet A22 at $I_{\text{coil}} = 0$ where $|I_{c+}| \approx |I_{c-}| \approx 8.43 \mu\text{A}$.

The normal resistance $R_N \approx 50 \Omega$ of our JJ roughly is determined by the slope at the current $I \approx 30 \mu\text{A}$ where the voltage is $V \approx 1.5 \text{ mA}$. It is worth noting that the observed bending near $|I| \approx \pm 32 \mu\text{A}$ may stem from a small distance between the two resistive walls w . Consequently, it is possible that some crystal destruction of YBCO has already occurred, leading to a quasi-junction in series with JJ of the ratchet, this results a bending phenomena at the $I \approx \pm 32 \mu\text{A}$. However, the exact cause cannot be determined with the absolute certainty.

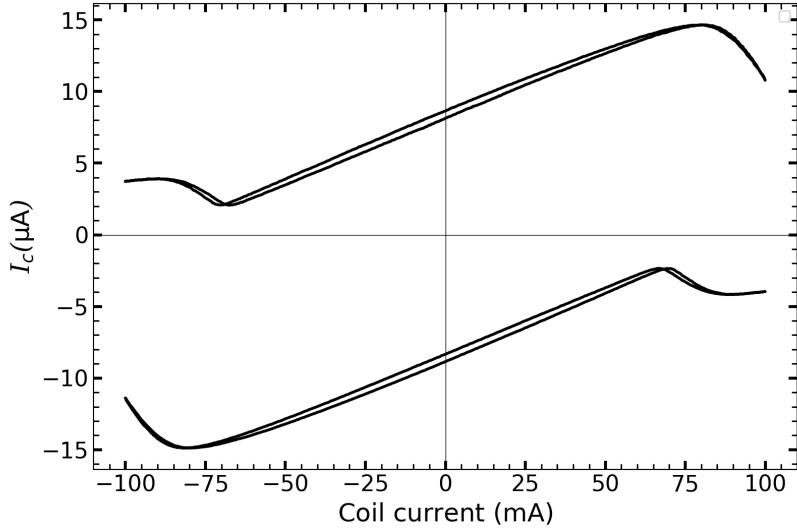


Figure 4.2: Critical current versus magnetic coil current of the Josephson ratchet A22. We used a voltage criterion equal to $1 \mu\text{V}$ for this measurement.

The dependencies of $I_c(I_{\text{coil}})$ is shown in the fig. 4.2. The coil current I_{coil} generates magnetic field H perpendicular to the sample plane and the coil factor we used for our measurement is approximately 0.17 mT/mA . Within our coil current range between $\pm 100 \text{ mA}$, we can clearly observe the skewed nature of $I_c(I_{\text{coil}})$. Using the fig. 4.2, we can identify the optimal magnetic field for which the asymmetry parameter \mathcal{A} has a maximum. To determine the dependence of asymmetry parameters (see eq. (2.1)) we have plotted $\mathcal{A}(I_{\text{coil}})$ as shown in the fig. 4.3

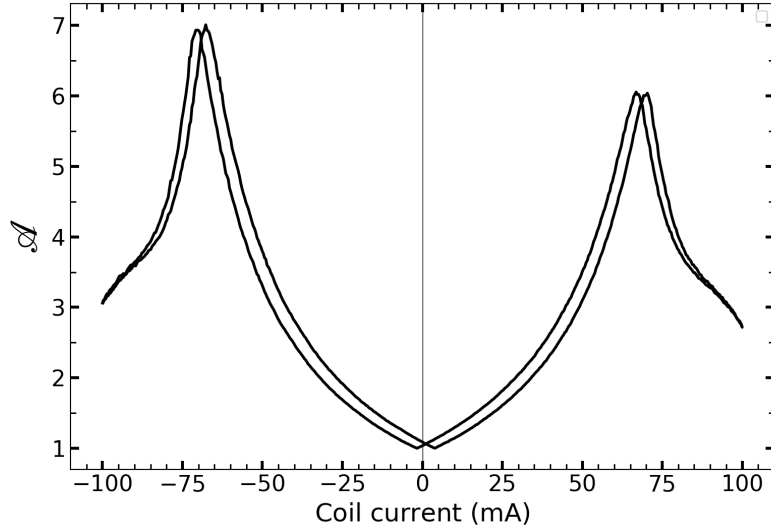


Figure 4.3: Value of asymmetry parameter dependence of I_{coil} , which shows the maximum asymmetry, is $\mathcal{A} \approx 7$ at the value of $I_{\text{coil}} \approx -69$ mA.

We have observed that \mathcal{A} is somewhat asymmetric with respect to polarity of I_{coil} . For instance, $\mathcal{A}(69 \text{ mA}) \approx 6$ whereas $\mathcal{A}(-69 \text{ mA}) \approx 7$. This asymmetry can be attributed to several factors; such as the shift of zero for the current source used to bias the JJ or the design of our ratchet itself.

Another issue, which we want to point out, concerns the discrepancy between the theoretically predicted \mathcal{A} and the experimental results \mathcal{A} . As we briefly mentioned in page. 22, this difference is mainly due to our choice of voltage criterion and many possible noise sources, e.g., voltage noises, internal, and external noises which we will explain in detail later on this chapter. These two main reasons causes the I_c at the optimum point in fig. 4.2 not to be close to zero in the direction of current, and therefore, \mathcal{A} is not so close to its theoretical prediction. For example, if we could reduce the thermal and other external source of noises, the I_{c+} in the optimum point ($I_{\text{coil}} \approx -69$ mA) would be much closer to zero and subsequently makes of the experimental value of \mathcal{A} much closer to its theoretical prediction. Another possible reason for such a differences is that e.g., our experimental I_c , see fig. 4.2, looks qualitatively different with its theoretical simulation fig. 2.9. For example, the minimum and maximum of I_c in the fig. 2.9 for $f^M > 0.9$ corresponds to the same value of coil current but in the experiment they are not. Hence one can expect such a differences of \mathcal{A} in the theory and experiments.

At this point, looking at fig. 4.3, the important point for us is to find the optimum I_{coil} where \mathcal{A} has a maximum. Once we find the optimum magnetic field, we can apply it to our device and measure the experimental asymmetric IVC as it is shown in fig. 4.4.

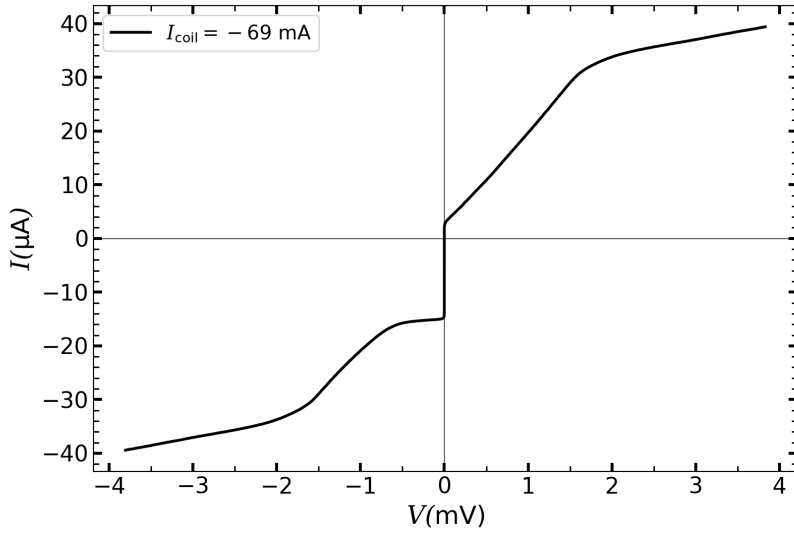


Figure 4.4: asymmetric IVC of the ratchet A22 at the optimum magnetic field (coil current) $I_{\text{coil}} = -69 \text{ mA}$ exhibits $|I_{c+}| \approx 1.53 \mu\text{A}$ and $|I_{c-}| \approx -13.8 \mu\text{A}$ that makes $\mathcal{A} \approx 7$.

Having such an asymmetric IVC we can now apply some ac-drive, which is defined by

$$I(t) = I_{\text{ac}} \sin \omega t, \quad (4.1)$$

and measure the rectification curve $\bar{V}_{\text{dc}}(I(t))$ as follows

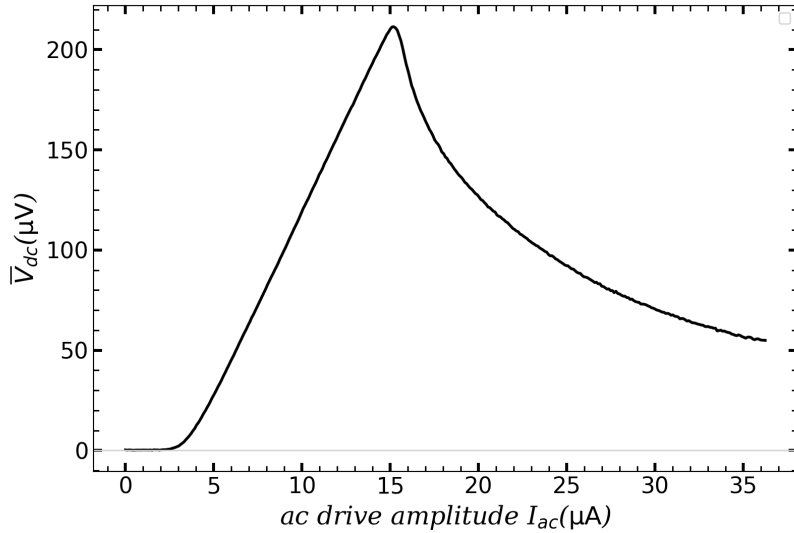


Figure 4.5: The rectification curve for the ratchet A22 at $I_{\text{coil}} = -69 \text{ mA}$ where $|I_{c-}| \approx 15.2 \mu\text{A}$, $|I_{c+}| \approx 2.2 \mu\text{A}$ and RW $\Delta \approx 13 \mu\text{A}$.

The rectification curve is experimentally measured over 5 ms, which corresponds to one period of the drive.¹ This curve is shown in the fig. 4.5. One can investigate the \bar{V}_{dc} from the asymmetric IVC fig. 4.4 as follows: for a small amplitude of ac-drive $I_{ac} < |I_{c_+}|$, V remains zero in the fig. 4.4 so the particle does not move and \bar{V}_{dc} remains zero in the fig. 4.5, when the ac-drive amplitude reaches to $|I_{c_+}| \approx 2.2 \mu\text{A}$, the particle starts moving and rectification has been occurring. By increasing the amplitude of ac-drive more the particle reaches to its maximum average velocity $\bar{V}_{dc} \approx 215 \mu\text{V}$ when the ac-drive amplitude is about to reach $|I_{c_-}| \approx 15.2 \mu\text{A}$. Then from that point on the average voltage starts decreasing to approach zero. However, until now our ratchet is still idle. To make it not idle, we will load it by applying some counterforce I_{dc} (which is equivalent to tilting the potential) in the opposite direction of the ratchet motion. This will compel the particle to climb uphill, which is due to the ratchet effect, and generate some useful work. The rectification curve, depicting the operation of loaded ratchet for different values of I_{dc} , is given by the fig. 4.6,

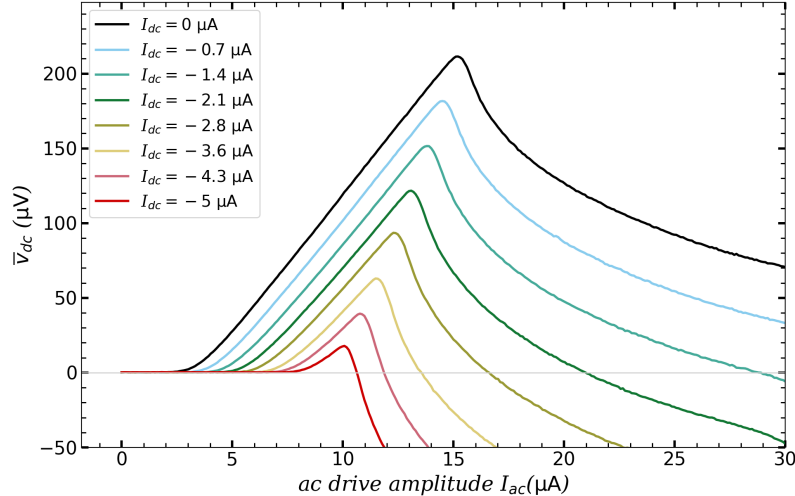


Figure 4.6: The rectification curve for the ratchet A22 at $I_{coil} = -69 \text{ mA}$ for several I_{dc} up to $|I_{dc}| = 5 \mu\text{A}$.

We observe that by increasing the absolute value of the counterforce, the RW shrinks until it closes at the stopping force around $|I_{dc}| \approx 5 \mu\text{A}$. After that, the speed of the particle gradually decreases. The value of stopping force is given by I_{stop} as $I_{stop} = \frac{|I_{c_-}| - |I_{c_+}|}{2}$ [4]. In our case, we obtained a value of approximately $-6.1 \mu\text{A}$ for I_{stop} , which closely aligns with our experimental finding of around $-5.5 \mu\text{A}$.

Now we can move on to measure the output power \bar{P}_{out} by multiplying $\bar{V}_{dc}(I(t))$ with the corresponding values of I_{dc} as e.g., $\bar{P}_{out} = \langle VI(t) \rangle \times I_{dc} = \bar{V}_{dc} \cdot I_{dc}$. Then

¹For our measurement setup, we employed 500 samples per period and $f = 200 \text{ Hz}$, and so sampling rate equal to $100K$ sample per second.

we measure the input power $\bar{P}_{\text{in}} = \langle V(I(t)) \times I(t) \rangle$ for the applied ac-drive. And finally, The efficiency from our experimental data is calculated. The dependence of \bar{P}_{in} , \bar{P}_{out} , and η on $I(t)$ respectively are given by fig. 4.7,

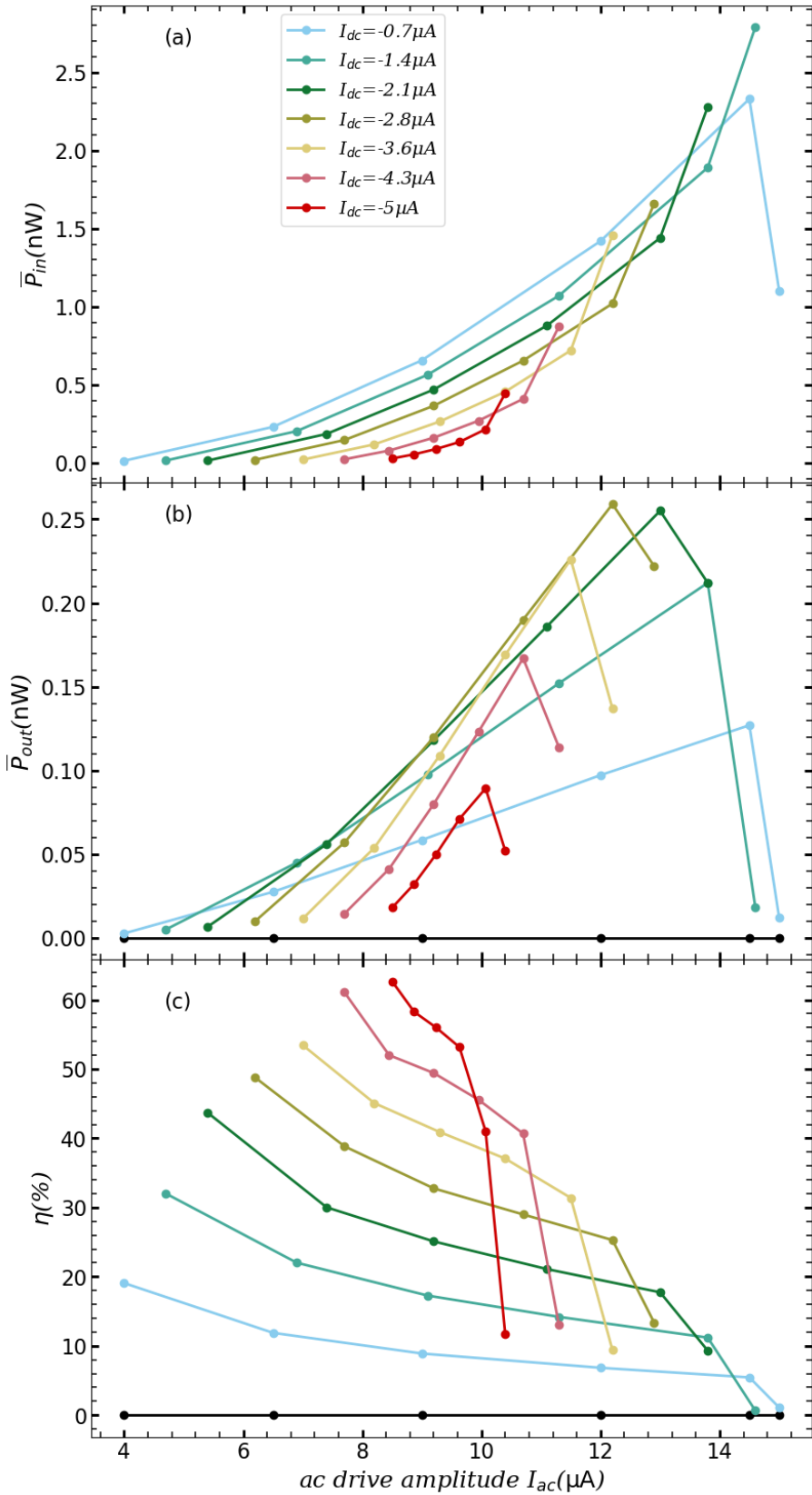


Figure 4.7: (a) $\bar{P}_{in}(I)$, (b) $\bar{P}_{out}(I)$, (c) efficiency $\eta(I)$.

To measure \bar{P}_{out} , we just simply multiply each \bar{V}_{dc} value by its corresponding I_{dc} . However, measuring \bar{P}_{in} presented a slightly more challenging situation as we were unable to pull $I(t)$ out of the average or integral similar to what we did with I_{dc} for \bar{P}_{out} . For each curves in the fig. 4.6 we choose six I_{ac} values, for which we made the following measurement manually. For each value we multiply $V(I(t)) \times I(t)$ and then integrated, specifically

$$\bar{P}_{\text{in}}(I(t)) = \frac{1}{T} \int_0^T V(I(t)) \cdot I(t) dt,$$

In the fig. 4.7(b), we observe that increasing I_{dc} leads to an increase in \bar{P}_{out} until $I_{\text{dc}} = -2.8 \mu\text{A}$. Further increases in I_{dc} cause a decrease in \bar{P}_{out} .

For efficiency fig. 4.7(c), we first observe that unlike \bar{P}_{out} , efficiency constantly increases by growing the values of I_{dc} , while the RW decreases. Furthermore, we note that for every values of I_{dc} , the maximum efficiency occurs at the beginning of the RWs, aligning with the predictions and simulations presented in Chapter 2.

In the next subsection, we will present the simulation results of the ratchet A22 and compare them with its corresponding experimental data.

4.2.1 Experimental Simulation of A22

In the quasistatic regime, the behaviour of the system is defined by the experimental IVC. Therefore starting from an experimental IVC, one can obtain all the figures of merit. To simulate $\bar{V}_{\text{dc}}(I(t))$, we took high resolution experimental asymmetric IVC, interpolate it and then we numerically calculate $\bar{V}_{\text{dc}} = \frac{1}{T} \int_0^T V(I(t) + I_{\text{dc}}) dt$ for the loaded ratchet as it is shown in fig. 4.8.

Next, we move on with \bar{P}_{in} , \bar{P}_{out} , and finally η , as given by fig. 4.9. Simultaneously, all the simulations are compared with whose corresponding experimental data.

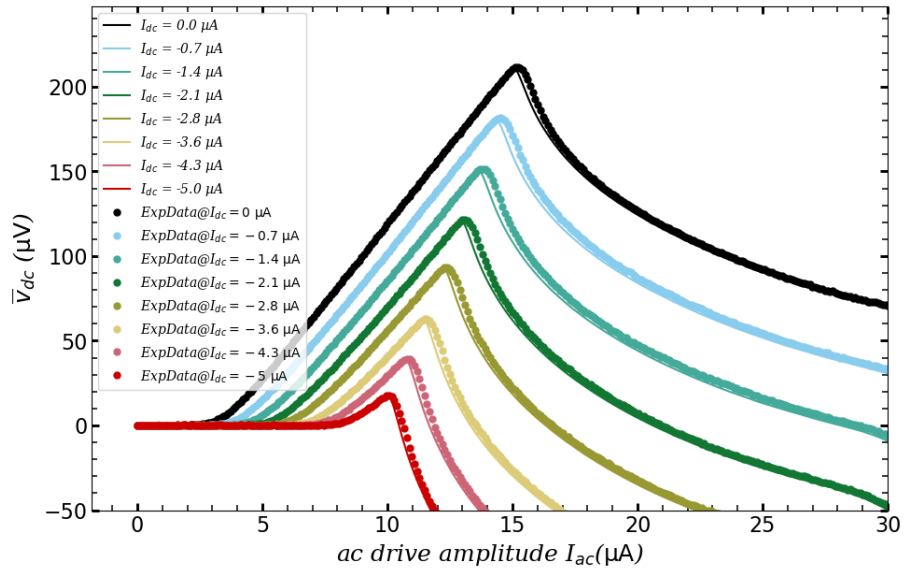


Figure 4.8: Simulations (lines) versus the experimental data (dots) of $\bar{V}_{dc}(I(t))$

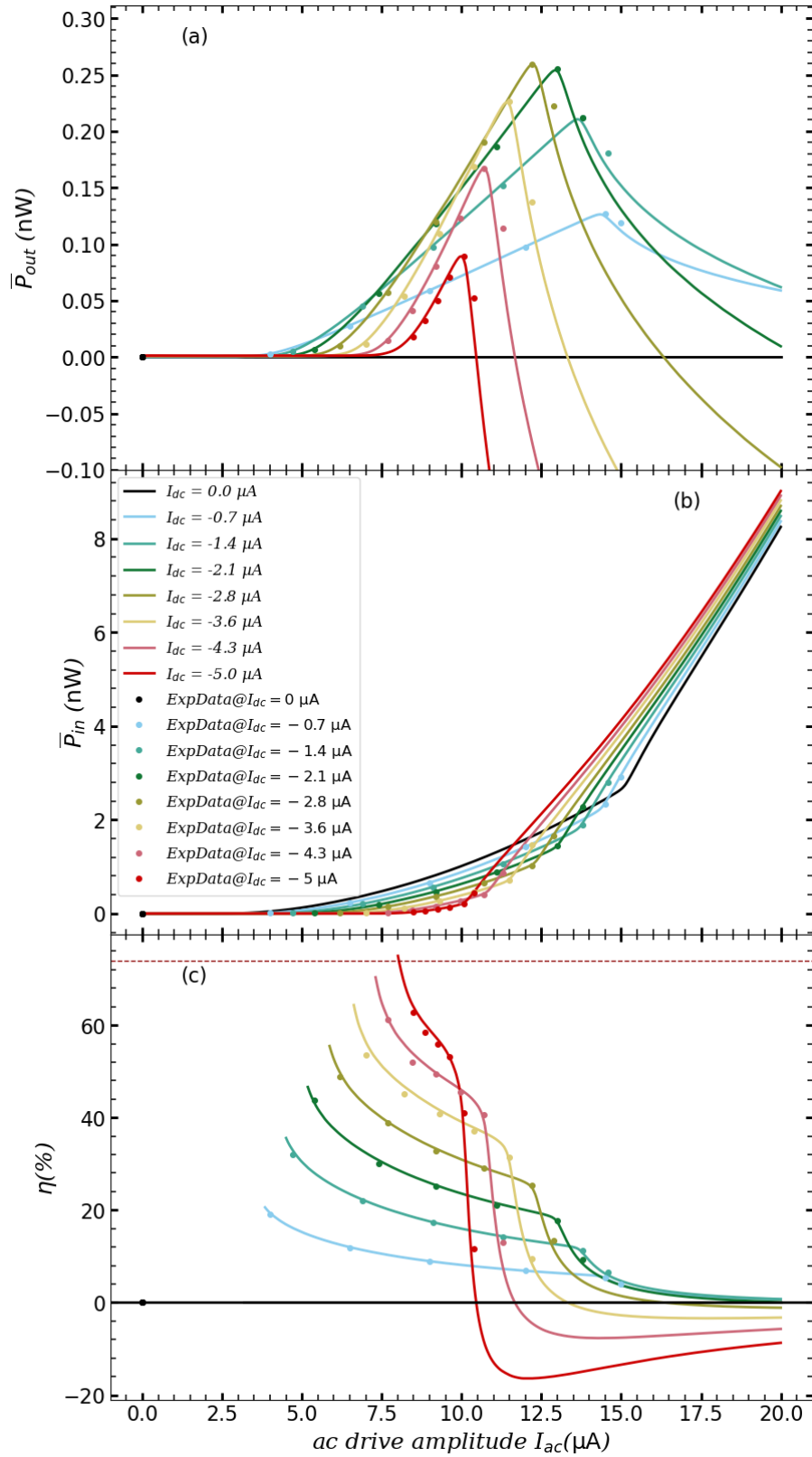


Figure 4.9: Simulations (lines) versus the experimental data (dots) of (a) $\bar{P}_{\text{in}}(I(t))$, (b) $\bar{P}_{\text{out}}(I(t))$, and (c) $\eta(I(t))$.

One important observation is that, for instance in the fig. 4.9, up to a current value of approximately $2\ldots 3\mu\text{A}$, the powers remain around zero, resulting in the efficiency tending towards infinity. To address this issue, we impose a cut-off criterion of $P_{\text{in}} \leq 10\text{ pW}$ to write our simulation code. Similarly in the experiment, we measured just the rectification window Δ , excluding one point outside, to capture the jump in the simulations of η in fig. 4.9(c).

Clearly, we observe that our experimental data are well coincided by our simulation results and the figures of merit. It is enlightening to mention that the theoretical maximum efficiency calculated in [4] (red dashed line in the fig. 4.9(c)) is around 74% which is nicely touches our maximum simulation curve. We also provide a comparison in the table. 4.3 to contrast our Josephson ratchet results with existing literature on the Josephson ratchet mechanisms.

4.3 Josephson Ratchet A15

In this section, we will present the experimental results for ratchet A15, similar to the previous section. A comparison between the actual and target parameters is provided in the table 4.2.

A15	Target parameter	Actual parameter
$w(\text{nm})$	300	300
Dose(ionS/nm)	507	507
$j_c (\text{kA}/\text{cm}^2)$	7.1	53
$I_c(\mu\text{A})$	3.7	28
$\lambda_j(\text{nm})$	250	129
$L(\text{nm})$	1750	1750
$l \equiv L/\lambda_j$	4.9	13.5
f^M	0.25	0.96
$\lambda_j^K(\text{nm})$	2960	1090
$l_K \equiv L/\lambda_j^K$	0.6	1.6
f_K^M	0.09	0.6

Table 4.2: Comparison table of target and actual parameters of ratchet A15.

The IVC of ratchet A15 is shown in the fig. 4.10

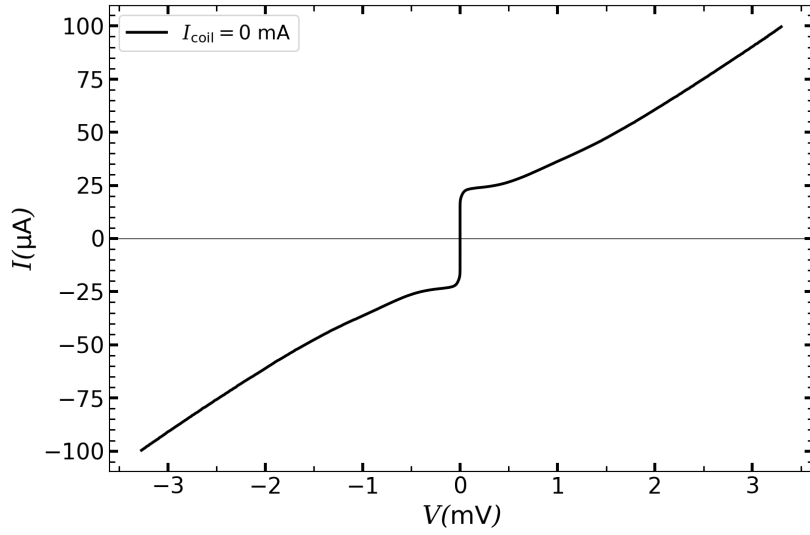


Figure 4.10: IVC of the ratchet A15 at $I_{\text{coil}} = 0$ mA. $|I_{c+}| = |I_{c-}| \approx 21 \mu\text{A}$ and $R_N \approx 32 \Omega$.

As we can clearly observe in fig. 4.10, there is no kink or bending in the IVC because we chose $w = 300 \text{ nm}$, and there is no crystal destruction of YBCO due to the distance between resistive walls. All the other experimental results for this ratchet similar to the Josephson ratchet A22 are presented in fig. 4.11 to 4.16

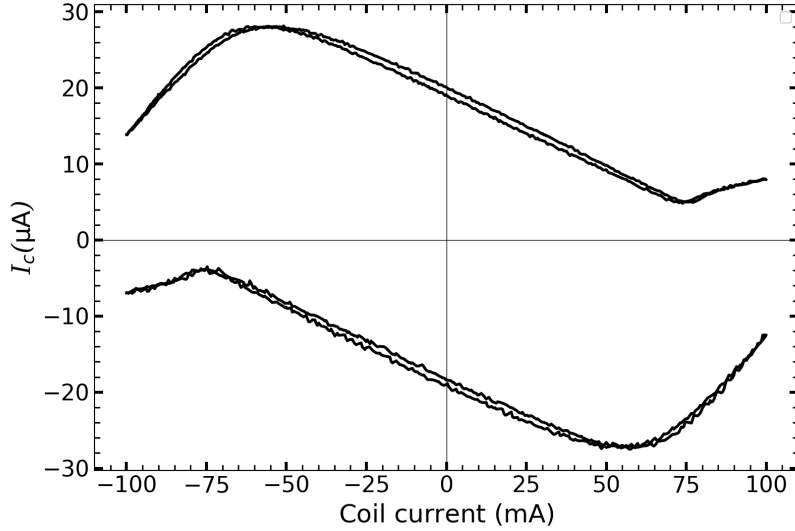


Figure 4.11: Critical current versus magnetic coil current of the ratchet A15.

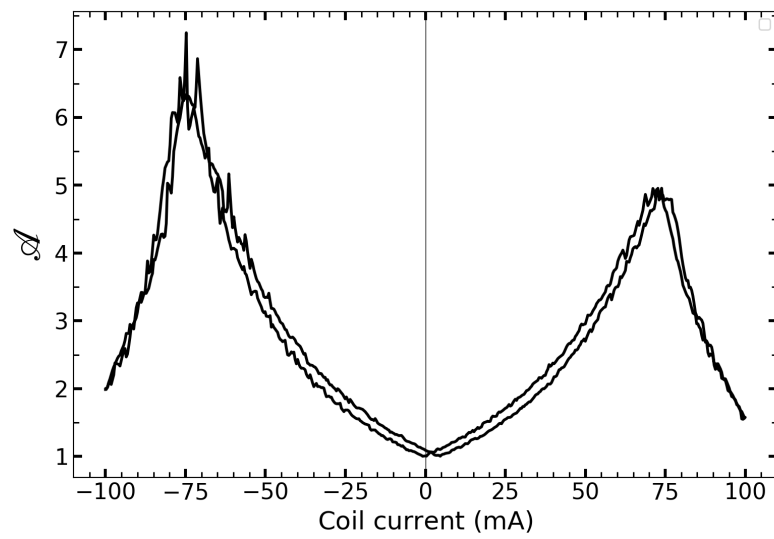


Figure 4.12: The value of asymmetry parameter, which shows the maximum asymmetry $\mathcal{A} \approx 7$ at optimum magnetic $I_{\text{coil}} = 75$ mA.

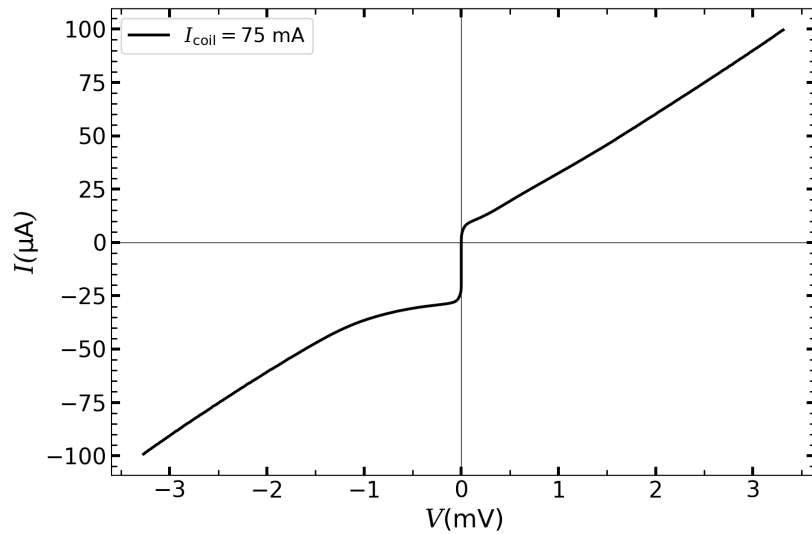


Figure 4.13: An asymmetric IVC of the ratchet A15 at the optimum $I_{\text{coil}} = 75$ mA has $|I_{c_-}| \approx 24.5 \mu\text{A}$ and $|I_{c_+}| \approx 3.5 \mu\text{A}$.

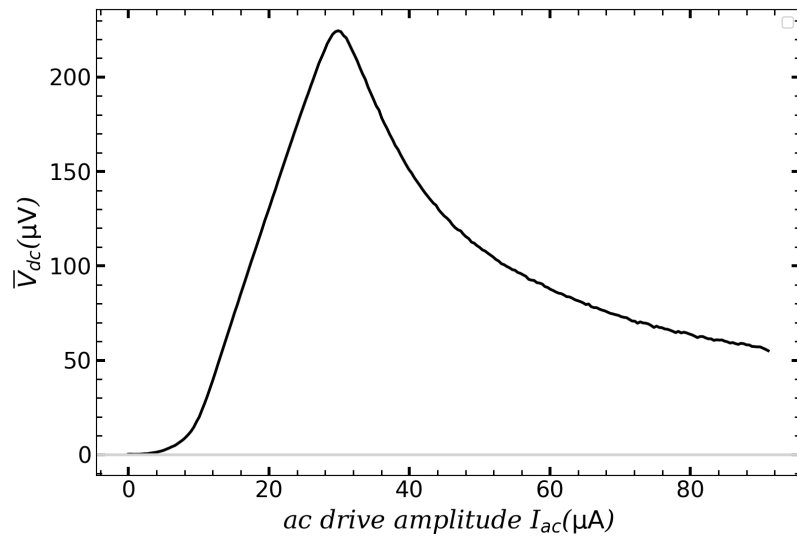


Figure 4.14: The rectification curve for the ratchet A15 at $I_{\text{coil}} = 75 \text{ mA}$ with maximum dc average voltage $\bar{V}_{dc} \approx 225 \text{ V}$.

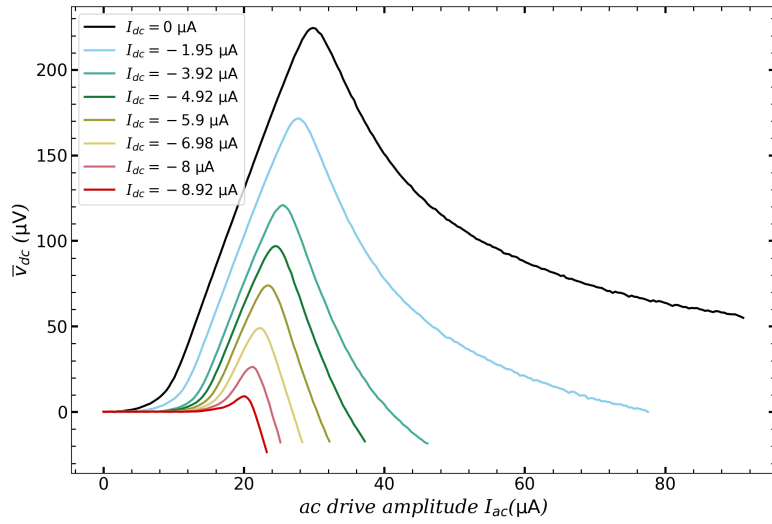


Figure 4.15: The rectification curve for the loaded ratchet A15 at $I_{\text{coil}} = 75 \text{ mA}$ for several I_{dc} up to stopping force $|I_{dc}| = 8.92 \mu\text{A}$.

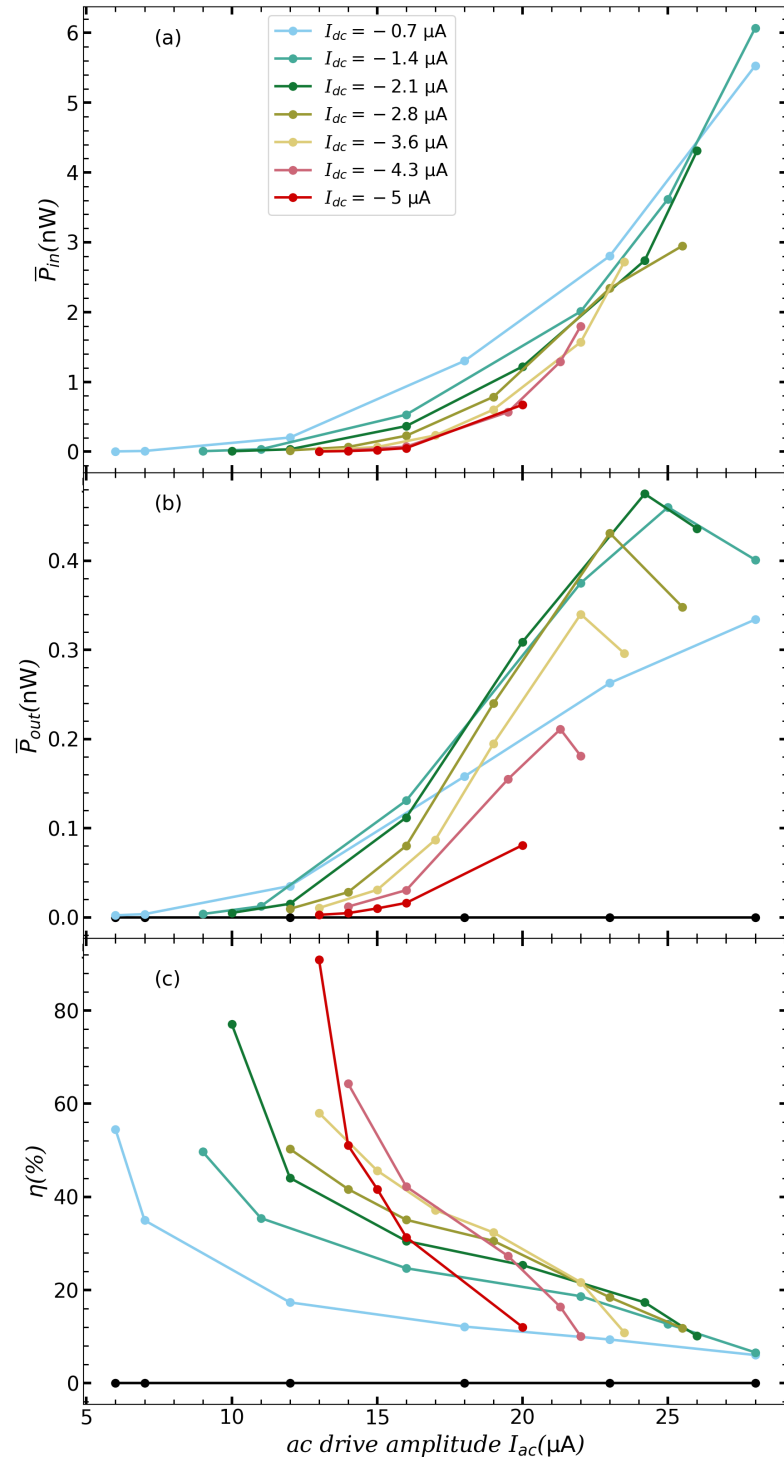


Figure 4.16: (a) \bar{P}_{in} , (b) \bar{P}_{out} , (c) efficiency η .

4.4 Driving the Ratchet with a Stochastic Signal

In this section, our objective is to examine the influence of different types of noise on the system and assess their impact on our system. In reality, numerous sources of noise can affect the system and diminish its accuracy. Therefore in this thesis, we explore two distinct approaches: external and internal noises.

To simulate external noise, we introduce random normal noises with a Gaussian distribution. For internal noise, we assume it consists of equilibrium thermal fluctuations, although there may be other sources of noise, such as white thermal noise, also known as $\frac{1}{f}$ noise or brown noise. These sources can include induced signals from radio stations, mobile devices, TV stations, satellites, and so on. Despite working in a screened room, it is not possible to completely eliminate the possibility of these noise sources. A schematic representation of the stochastic signal and its corresponding distribution can be found in the fig. 4.18,

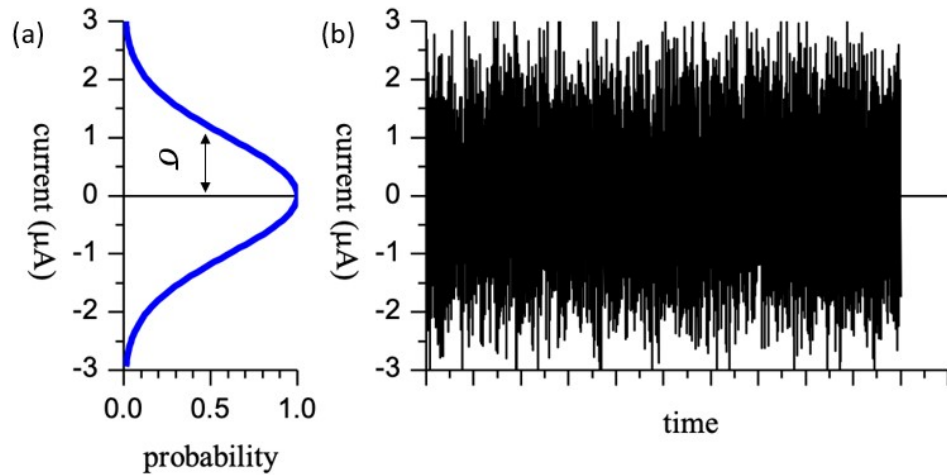


Figure 4.18: (a) The Gaussian distribution of random signal with the width σ (b) The random signal depends on time.

4.4.1 External noise

For the first case, our focus is on examining the impact of external noises by simulation. To accomplish this, we substitute the deterministic ac-drive with an external random signal to drive the ratchet system in a stochastic regime. Once again, since we are operating in the quasistatic regime, we can consider the high resolution experimental asymmetric IVC of A22 and simulate all the figures of merit by driving the system with the Gaussian signal. To perform the calculation, we employ a similar procedure to the one used for the ac-drive. However, since we do not have a periodic signal, it is necessary to average over a longer interval, therefore we consider the standard deviation $\sigma(I)$ as a measure of amplitude of our noisy signal. Nevertheless, due to the ergodicity of the noise, we can approximate this averaging process by convolution with a Gaussian distribution, as outlined below,²

$$(V * G)(\sigma) = \bar{V}(\sigma, I_{dc}) = \int_{\sigma_{min}}^{\sigma_{max}} V(I + I_{dc}) \cdot G(I, \sigma) dI = \sum_{i=0}^{M-1} V(I + I_{dc}) \cdot G(I, \sigma) \Delta I$$

where G is the Gaussian distribution and we chose $M = 812$ data points. Similarly we calculate $\bar{P}_{out}(\sigma, I_{dc}) = \bar{V}_{dc}(\sigma, I_{dc}) \cdot I_{dc}$ and $\bar{P}_{in}(\sigma, I_{dc}) = \int_{\sigma_{min}}^{\sigma_{max}} V(I + I_{dc}) \cdot G(I, \sigma) \cdot I(t) dI$. The simulated \bar{V}_{dc} , \bar{P}_{in} , \bar{P}_{out} , and efficiency η of the noisy driven ratchet are presented in the fig. 4.19 and fig. 4.20 respectively,

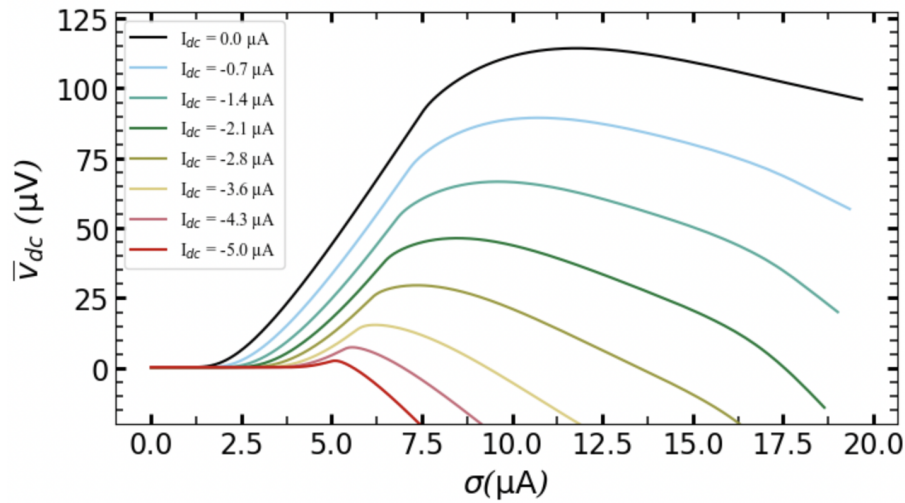


Figure 4.19: Simulation of $\bar{V}_{dc}(\sigma)$ driven with the Gaussian signal.

²It is important to note that the amplitude of the Gaussian signal is infinite and random. Therefore, we adopt the parameter $\sigma(I)$ as a measure of the amplitude of our noisy signal.

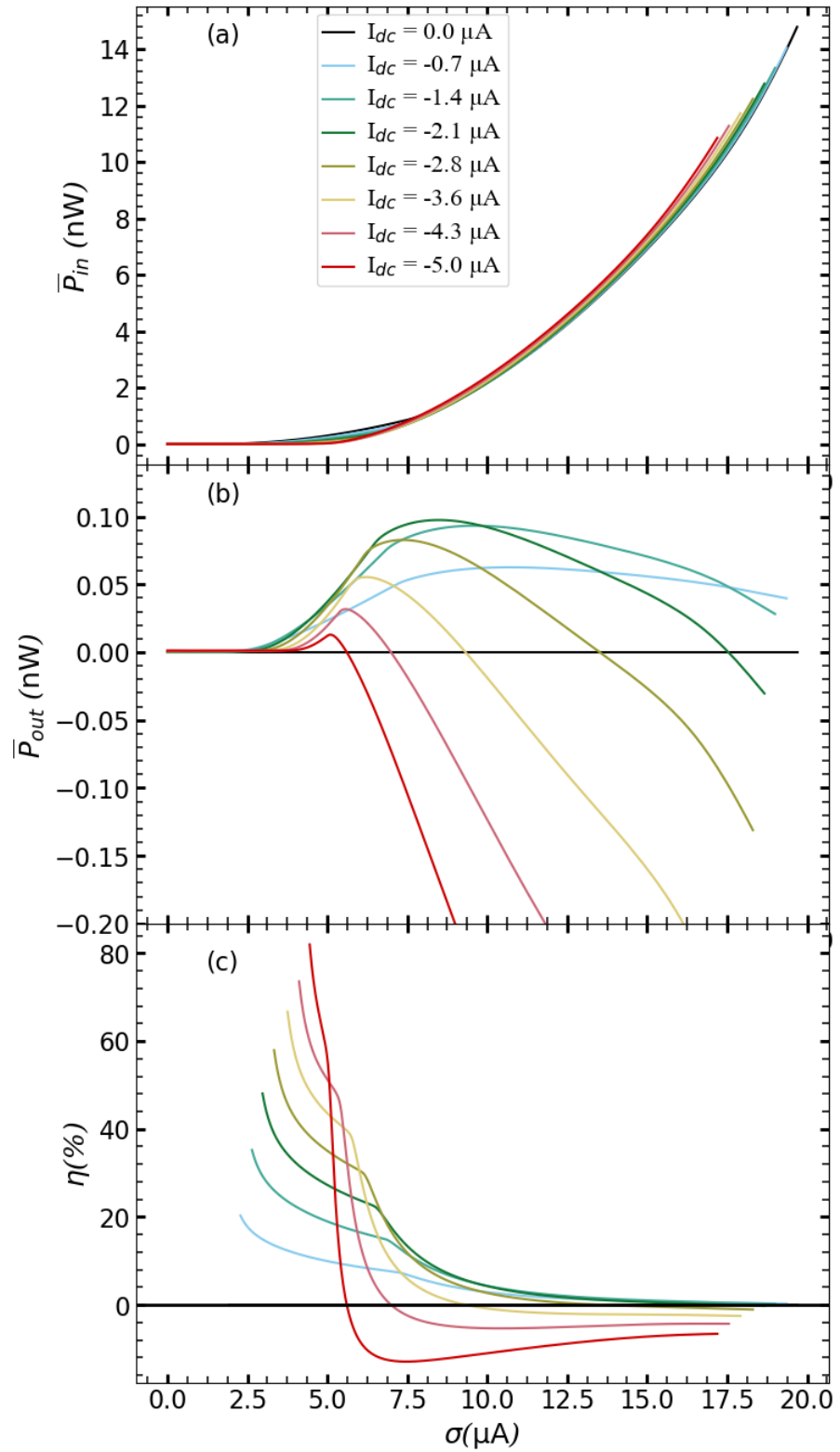


Figure 4.20: (a) $\bar{P}_{in}(\sigma)$, (b) $\bar{P}_{out}(\sigma)$, (c) and η

We observe that our Josephson ratchet system remains functional when driven by a random signal instead of a deterministic drive. The figures of merit obtained under the random signal exhibit a similar behavior to those achieved under the deterministic drive. However, it is worth noting that the maximum value of the average voltage \bar{V}_{dc} , decreases by a factor of two compared to deterministic drive (ac-drive). Thus, in principle, we drive the system with noise and observe that the noise can also facilitate the transfer of the particle, albeit at a slower pace.

4.4.2 Internal noise

For the case of internal noise, we utilize the inherent noise present within the system, commonly referred to as thermal noise. Thermal noise arises from the random fluctuations due to the thermal energy of the system, specifically in the shunt resistor at a finite temperature. These fluctuations exhibit an amplitude distribution that is nearly Gaussian. The fluctuation-dissipation theorem provides a generic and statistically derived explanation for this phenomenon in the field of statistical physics.

Due to the utilization of high-temperature superconductors (HTSs), our ratchet system can be operated at temperatures up to around 40K. At this temperature, the thermal energy ($k_B T$) is approximately ten times greater compared to when the temperature is 4K. Consequently, the ratchet can be operated with a significantly higher thermal energy level. In the following we present the IVC of the ratchet A15 at temperature around 4.2K and 35K.

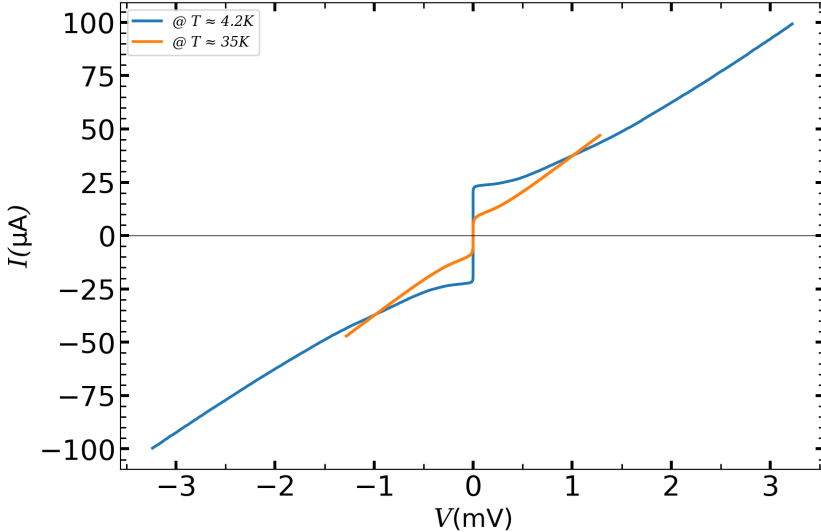


Figure 4.21: IVC of A15 at $T \approx 4.2$ K and 35 K at zero magnetic field $I_{\text{coil}} = 0$.

We observe that with increasing temperature, the critical current I_c decreases while thermal noise increases, $I_{\text{th}} = \frac{2\pi k_B T}{\Phi_0} \approx 1.4 \mu\text{A}$ at ≈ 30 K. Consequently, as we

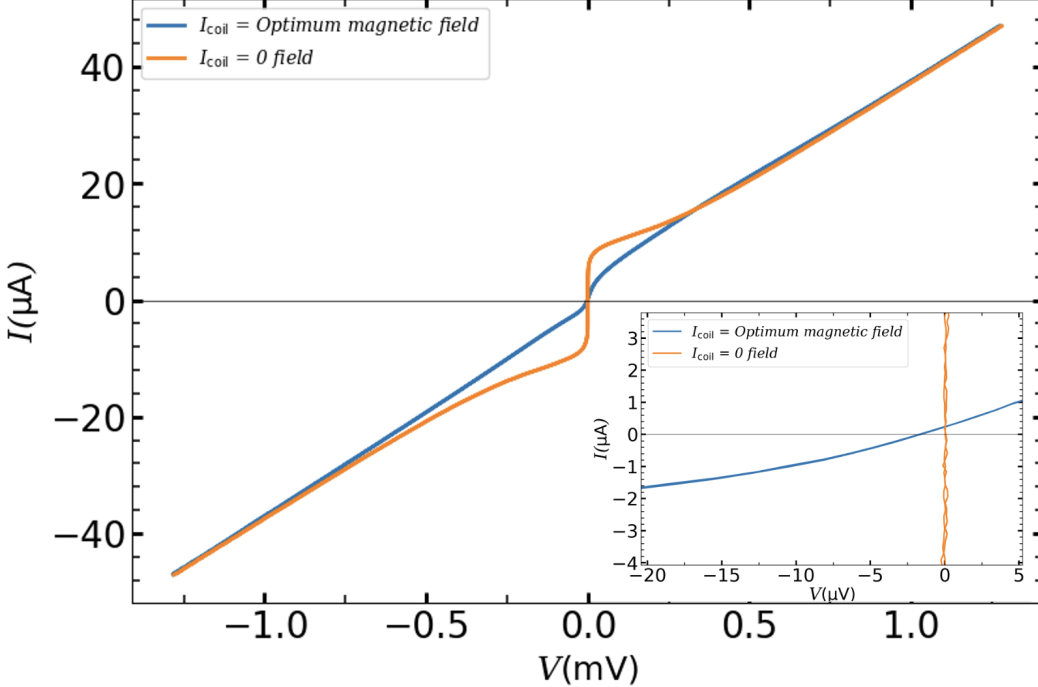


Figure 4.22: IVC for the ratchet A15 at around temperature 35K for the two values of I_{coil} : zero and the optimum magnetic field. In the lower right we zoom in the origin.

approach temperatures in the range of 30–40K, we reach to the point where thermal energy noise becomes comparable to the Josephson energy or thermal current becomes comparable with the critical current. Now by applying the optimum magnetic field across the device makes I_{c+} very small, smaller than the noise current and therefore strongly smeared on IVC, which can be characterized by the noise parameter $\Gamma = \frac{2\pi k_B T}{\Phi_0 I_0} = \frac{I_{\text{th}}}{I_c}$. [9] [12] Now the very important question is: will asymmetric IVC still cross the origin or it does not cross the origin due to the rounding around I_c and one will get $V(0) \neq 0$. The IVC at $H = 0$ and at H equal to optimum magnetic field at $T \approx 35\text{K}$ is shown in the fig. 4.22. Upon zooming in, we confirm that the critical current of the blue curve $I_c \approx 2\text{ }\mu\text{A}$ and indeed it does not cross the origin. Thus, the fact that it does not cross zero indicates that, the internal noise is rectified producing small dc voltage. However experimentally there can be many pitfalls. In particular case, the lack of crossing origin may potentially be attributed to the shift of zero of the current source. To check this, we disconnected the cable from the current source to JJ and perform an additional measurement, as depicted in fig. 4.23.

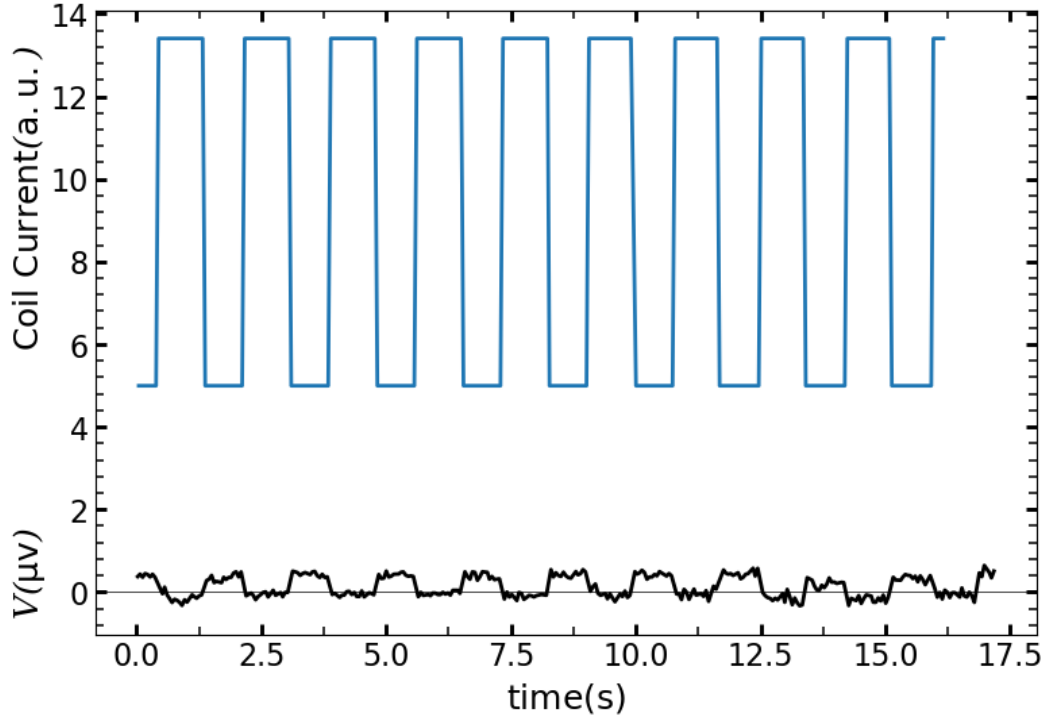


Figure 4.23

In this measurement, we recorded the voltage-versus-time $V(t)$ for device A15 for two cases: when the coil current I_{coil} was set to 0 and when it was set to the optimum value. It was observed that when $I_{\text{coil}} = 0$, there was no voltage response, whereas for the optimum magnetic field, a voltage of approximately $0.4 \mu\text{V}$ was observed. This voltage can be attributed to the rectification effect caused by the noise. Similar effect was observed in a SQUID two decades ago [12]. However, it is known that the second laws of thermodynamics forbids the rectification of equilibrium thermal fluctuation (white noise). Therefore the rectification is probably related to some non-equilibrium noise (i.e., $\frac{1}{f}$) or to induce noises from mobile, radio or TV networks (although our experiment was performed in the screening room). The investigation of the spectral properties of noise is a topic for future research that we would explore in our future work.

4.5 Conclusion and Outlook

Using He-FIB, we successfully operated the Josephson ratchets with an efficiency exceeding 74% based on asymmetry parameter $\mathcal{A} \approx 7$ and a maximum average rectified dc voltage $\bar{V}_{dc} \approx 215 \mu V$ with the area of JJ around $1 \mu m^2$. To our knowledge, these results establish a record value in the Josephson ratchet literature (see the table 4.3). We conducted several measurements and simulations where we drove the ratchet in both deterministic and stochastic regimes to determine the figures of merit i.e., \bar{V}_{dc} , \bar{P}_{out} , \bar{P}_{in} , and the efficiency η . Finally, we observed the effect of noises in our Josephson ratchet system, which resulted in a small amount of rectified dc voltage being captured in the highly non-equilibrium regions.

As an **Outlook** we have several tasks in mind. Most importantly a more detailed studies on the effects noises is required. In particular, the investigation of the spectrum rectified signal, the bandwidth at different noise parameters. To accomplish this, one should aim to fabricate the Josephson ratchets with smaller dimensions and lengths, and maximizing the asymmetry parameters \mathcal{A} .

Second by achieving a significant number of well-performing ratchets (for example, enhancing the quality of BJJs and minimizing the spread of j_c), one can construct an array of Josephson ratchets to obtain more rectified dc voltage.

Third, one would develop a new generation of SQUIDs based on in-line geometry of JJ with a periodic asymmetric potential. Surpassing the capabilities of simple Josephson junctions with symmetric potential and investigating the different probable effect of the periodic asymmetric potential into the system at nano scale.

References	Kind	\mathcal{A}	$\bar{V}_{dc}(\mu V)$	$\bar{P}_{out}(nW)$	$\bar{P}_{in}(nW)$	$\eta(\%)$	Area (μm^2)	$T_{op}(K)$
Carapella (2001) [13]	ALJJ	1.2	5	-	-	-	44500	6.5
Beck (2005) [14]	ALJJ	2.2	20	-	-	-	5700	6
Strek (2005) [15]	3JJ SQUID	2.5	25	-	-	-	7, 15	4.2
Strek (2009) [12]	3JJ SQUID	2	25	-	-	-	5.3, 11.3	4.2
Wang (2009) [16]	ALJJ	2.8	100	-	-	-	800	4.2
Knufinke (2012) [1]	ALJJ	4	40	1.5-2.5	4-10	60	1300, 5700	4.2
Menditto (2016) [17]	φ junction	2.5	150	-	-	-	2000	1.7
Golod (2022) [3]	J Diod	3	8	-	-	60	$L = 5.6$	7
Paolucci (2023) [18]	SQUID Diod	3	8	-	-	70	Dayem bridges	50-400mK
My thesis (2023)	J ratchet	7	215	0.001-0.2	0.1-2	74	0.9	4.2

Table 4.3: Comparison table of important parameters for a system with a periodic asymmetric potential. ALJJ is the abbreviation of annular long JJ, and SQUID is the abbreviation of superconducting quantum interference device. Note that in the ref Knufinke et al [1].., they just obtained \bar{V}_{dc} experimentally, while simulating all the other parameters using a custom-made asymmetric IVC.

References

- [1] M. Knufinke, K. Ilin, M. Siegel, D. Koelle, R. Kleiner, and E. Goldobin. "Deterministic Josephson vortex ratchet with a load", Jan 2012. *Phys. Rev. E* **85**, 011122 (2012).
- [2] Peter Reimann. "Brownian motors: noisy transport far from equilibrium", Apr 2002. *Elsevier, Volume 361, Issues 2–4.* (2002).
- [3] Taras Golod and Vladimir M. Krasnov. "Demonstration of a superconducting diode-with-memory, operational at zero magnetic field with switchable nonreciprocity", Jun 2022. *Nature Communication, volume 13, 3658.* (2022).
- [4] E. Goldobin, R. Menditto, D. Koelle, and R. Kleiner. "Model I–V curves and figures of merit of underdamped deterministic josephson ratchets", Sep 2016. *Phys. Rev. E* **94**, 032203 (2016).
- [5] Josephson effect. [Wikipedia](#).
- [6] Roderich Tumulka. "Foundations of Quantum Mechanics", Nov 2022. [Springer \(2022\)](#).
- [7] Ginzburg–Landau theory. [Wikipedia](#).
- [8] Antonio Barone. "Physics and applications of Josephson effect", 1982.
- [9] Dieter Kölle. "Basic Properties of Josephson Junctions". [Koelle's Slides.](#) (2019).
- [10] Jodie Roderiguez. "Characterization of Josephson junctions created by he+ irradiation in commercial Ceraco $\text{YBa}_2\text{Cu}_3\text{O}_{7-x}$ thin films", 2022. Bachelor thesis.
- [11] B. Müller, M. Karrer, F. Limberger, M. Becker, B. Schröppel, C.J. Burkhardt, R. Kleiner, E. Goldobin, and D. Koelle. "Josephson Junctions and SQUIDS Created by Focused Helium-Ion-Beam Irradiation of $\text{YBa}_2\text{Cu}_3\text{O}_7$ ", Apr 2019. *Phys. Rev. Applied* **11**, 044082 (2019).
- [12] Kleiner R. Sterck A, Koelle D. "Rectification in a stochastically driven three-junction squid rocking ratchet", Jul 2009. *Phys. Rev. Lett.* **103**, 047001 (2009).
- [13] G. Carapella and G Costabile. "Ratchet effect: Demonstration of a Relativistic Fluxon diode", Jul 2001. *Phys. Rev. Lett.* **87**, 077002 (2001).

- [14] M. Beck, E. Goldobin, M. Neuhaus, M. Siegel, R. Kleiner, and D. Koelle. "High-Efficiency Deterministic Josephson Vortex Ratchet", Aug 2005. *Phys. Rev. Lett.* **95**, 090603 (2005).
- [15] A. Sterck, R. Kleiner, and D. Koelle. "Three-junction SQUID Rocking Ratchet", Oct 2005. *Phys. Rev. Lett.* **95**, 177006 (2005).
- [16] H. B. Wang, B. Y. Zhu, C. Gürlich, M. Ruoff, S. Kim, T. Hatano, B. R. Zhao, Z. X. Zhao, E. Goldobin, D. Koelle, and R. Kleiner. "Fast Josephson vortex ratchet made of intrinsic Josephson junctions in $\text{Bi}_2\text{Sr}_2\text{CaCu}_2\text{O}_8$ ", Dec 2009. *Phys. Rev. B* **80**, 224507 (2009).
- [17] R. Menditto, H. Sickinger, M. Weides, H. Kohlstedt, D. Koelle, R. Kleiner, and E. Goldobin. "Tunable φ Josephson junction ratchet", Oct 2016. *Phys. Rev. E* **94**, 042202 (2016).
- [18] F. Giazotto F. Paolucci, G. De Simoni. "A gate- and flux-controlled supercurrent diode effect", Jan 2023. *Appl. Phys. Lett.* **122**, 042601 (2023).